Partie VI

Conclusion et perspectives

Conclusion et perspectives

L E BUT INITIAL DE CE TRAVAIL ÉTAIT d'obtenir une meilleure caractérisation de la turbulence pouvant apparaître dans les disques d'accrétion, afin d'aboutir à une description précise du transport turbulent. Pour ce faire, j'ai envisagé plusieurs instabilités comme sources potentielles de turbulence :

- **Instabilité sous-critique hydrodynamique.** Pour traiter le cas de cette instabilité, j'ai développé un code spectral, tridimensionnel et incompressible afin d'obtenir des simulations dans lesquelles la dissipation numérique était contrôlée. Ce code a permis de montrer que le transport turbulent induit par cette instabilité était très probablement trop faible pour expliquer le transport observé dans les disques.

Une des originalités de ce travail a été l'étude poussée des différents biais numériques : résolution, rapport d'aspect, conditions aux limites et algorithme d'intégration ont été modifiés pour tester leur impact sur le résultat final. De plus, j'ai utilisé de manière explicite une dissipation physique dans les simulations, ce qui a permis de mettre en évidence les problèmes de convergence et de les maîtriser.

Enfin, des résultats expérimentaux postérieurs à mes propres travaux (Ji *et al.* 2006) ont montré des conclusions similaires, signant probablement la fin de l'instabilité sous-critique comme source de turbulence dans les disques d'accrétion.

- **Instabilité strato-rotationnelle.** J'ai étudié cette instabilité hydrodynamique de manière essentiellement analytique, par une approche asymptotique. J'ai dans un premier temps dérivé un critère d'instabilité pour les solutions les plus simples, en considérant des conditions aux limites «variables», pouvant reproduire par exemple les conditions aux limites rigides ou libres. J'ai ainsi montré que ces solutions n'étaient pas pertinentes pour les disques d'accrétion, car très dépendantes des conditions aux limites radiales.

J'ai par la suite étudié les solutions dites «oscillantes» par un raccordement asymptotique à travers plusieurs domaines d'approximation. J'ai ainsi montré que ces solution étaient instables lorsqu'elles étaient placées dans des conditions aux limites rigides.

Enfin, un code numérique aux différences finies d'ordre élevé, dont j'avais commencé le développement pour l'étude de l'instabilité sous-critique, a été utilisé. J'ai ainsi mis en évidence cette instabilité numériquement, et j'ai montré que l'abandon des conditions aux limites rigides pour des conditions shearing sheet entraînait la disparition de l'instabilité. Tous ces arguments tendent donc à montrer que cette instabilité est de nature globale, et peu ou pas pertinente d'un point de vue astrophysique.

Il reste cependant à obtenir un critère générique d'instabilité, qui soit indépendant du type de solution considéré. Ce critère permettrait alors d'obtenir une réponse définitive à la pertinence de la SRI dans les disques.

• **Instabilité magnéto-rotationnelle.** Pour débuter l'étude de cette instabilité, j'ai dérivé les critères d'instabilité linéaire dans différentes limites, en considérant une viscosité et une résistivité moléculaire. Ce type de critère n'est pas réellement nouveau, mais les limites analytiques obtenues permettent d'avoir un point de vue clair et complet sur le rôle des phénomènes dissipatifs dans cette instabilité.

J'ai poursuivi cette étude en développant une extension MHD du code spectral utilisé pour l'instabilité sous-critique. Suivant la logique de ce premier travail, j'ai cherché à comprendre quel était le rôle des nombres sans dimensions sur le processus de saturation de la MRI. J'ai ainsi montré un phénomène de bouffées turbulentes apparaissant au voisinage du seuil en champ fort de l'instabilité linéaire. Cependant, l'implication de ce résultat pour la physique des disques est encore obscure, et le rôle des conditions aux limites, de la compressibilité et de la stratification verticale restent à clarifier.

Je me suis enfin attaché à étudier le rôle des effets dissipatifs visqueux et résistifs sur la saturation de la turbulence MRI, ce qui avait été jusqu'à présent négligé. Bien que la saturation semble dépendre peu des effets dissipatifs à Prandtl constant, il semble que la variation de ce dernier entraîne des variations notables du coefficient de transport. De plus, dans le cas sans champ magnétique vertical imposé, il semble que la turbulence disparaisse dans les cas où $Pm \lesssim 1$. Ce point met alors en doute une partie de la littérature utilisant cette topologie du champ magnétique sans contrôler les effets dissipatifs.

Les implications astrophysiques de ces résultats sont encore à discuter, notamment en raison des facteurs d'échelle mis en jeu entre les simulations et les disques d'accrétion réels. Il n'en reste pas moins qu'une compréhension approfondie du phénomène de saturation de la MRI, en fonction notamment des paramètres sans dimensions contrôlant la dissipation, semble être un point *sine qua non* pour pouvoir développer un jour un modèle physiquement pertinent de transport turbulent dans les disques.

Vu ces résultats, plusieurs pistes de recherches peuvent être proposées :

- Étudier les effets de la stratification sur le phénomène de bouffée turbulente. Dans ce but, j'ai développé une version MHD du code différences finies utilisé ici. Remarquons cependant que la présence d'un champ magnétique vertical dans un écoulement stratifié pose de nombreux problèmes numériques (voir par exemple Stone *et al.* 1996) qu'il conviendra de résoudre.
- Créer un modèle sous maille type LES (*Large Eddy Simulation*) avec des simulations numériques locales, afin de pouvoir incorporer les effets de la turbulence dans des simulations à grande échelle. Ce type d'approche présente cependant plusieurs difficultés. En effet, les approches LES ont été beaucoup moins développées et testées dans le cas MHD que dans le cas hydrodynamique. Il faudra donc probablement créer de nouveaux modèles de clôture sous-maille si on envisage une telle approche. De plus, les simulations numériques locales actuelles ne sont pas suffisamment résolues pour montrer clairement un spectre inertiel, lequel est requis pour pouvoir utiliser la séparation d'échelle d'une LES. Aussi, des moyens numériques très performants seront nécessaires pour utiliser cette approche dans les disques d'accrétion.
- Étudier l'effet dynamo potentiellement à l'œuvre dans la MRI. Les simulations numériques sans flux net semblent montrer que l'instabilité survit et maintient des

fluctuations de champ magnétique pendant plusieurs milliers de temps dynamique lorsque $Pm > 1$. Un point important serait de savoir s'il s'agit là d'un réel effet dynamo, et, si tel est le cas, si cet effet peut être à l'origine d'un champ magnétique à grande échelle, susceptible d'être le vecteur des phénomènes d'éjection et de collimation des jets.

————–

Partie VII

Annexes

A
L'approximation de Hill

Plan du chapitre

1. Dérivation du modèle local de Hill

§ 88. Pression et tension magnétique

Tout d'abord, notons que dans le système d'équations MHD, on peut réécrire la force de Lorentz ainsi que l'équation d'induction sous la forme :

$$\frac{(\boldsymbol{\nabla} \times \boldsymbol{B}) \times \boldsymbol{B}}{4\pi} \;\; = \;\; -\boldsymbol{\nabla}\frac{B^2}{8\pi} + \frac{1}{4\pi}\boldsymbol{B}\cdot\boldsymbol{\nabla}B \tag{88.326}$$

$$\frac{\partial \boldsymbol{B}}{\partial t} + \boldsymbol{V}\cdot\boldsymbol{\nabla}B \;\; = \;\; \boldsymbol{B}\cdot\boldsymbol{\nabla}V - B(\boldsymbol{\nabla}\cdot\boldsymbol{V}) + \eta\Delta B \tag{88.327}$$

La force de Lorentz fait ainsi apparaître un terme de pression magnétique et un terme de tension magnétique agissant lorsque les lignes de champ sont courbées. De plus on obtient pour l'équation d'induction une formulation reflétant, d'une part, le transport du champ magnétique par le champ de vitesse, et d'autre part, un terme d'élongation des tubes de champ, similaire à l'équation de vorticité que l'on peut obtenir en hydrodynamique.

§ 89. Développement des équations en coordonnées cylindriques

On se place dans un référentiel cylindrique (r, ϕ, z) avec pour origine l'objet central et l'axe vertical perpendiculaire au plan médian du disque d'accrétion. On ajoute de plus à l'équation du mouvement (7.49) un potentiel gravitationnel dû à l'objet central[30] $\psi(r, z)$. La projection sur

---

[30]Le potentiel d'auto gravité dû au disque sera négligé en raison de la très faible masse du disque comparativement à l'objet central (Lin & Papaloizou 1996).

les trois composantes e_r, e_ϕ, e_z de l'équation du mouvement (7.49) donne alors :

$$\left(\frac{\partial}{\partial t} + \boldsymbol{V} \cdot \boldsymbol{\nabla}\right)V_r - \frac{V_\phi^2}{r} = -\frac{1}{\rho}\frac{\partial}{\partial r}\left(P + \frac{B^2}{8\pi}\right) - \frac{\partial \psi}{\partial r}$$

$$+\frac{1}{4\pi\rho}\boldsymbol{B} \cdot \boldsymbol{\nabla}B_r - \frac{B_\phi^2}{4\pi\rho r} + \frac{1}{\rho}(\boldsymbol{\nabla} \cdot \boldsymbol{\mathcal{T}})_r \qquad (89.328)$$

$$\left(\frac{\partial}{\partial t} + \boldsymbol{V} \cdot \boldsymbol{\nabla}\right)V_\phi + \frac{V_\phi V_r}{r} = -\frac{1}{\rho r}\frac{\partial}{\partial \phi}\left(P + \frac{B^2}{8\pi}\right)$$

$$+\frac{1}{4\pi\rho}\boldsymbol{B} \cdot \boldsymbol{\nabla}B_\phi + \frac{B_\phi B_r}{4\pi\rho r} + \frac{1}{\rho}(\boldsymbol{\nabla} \cdot \boldsymbol{\mathcal{T}})_\phi \qquad (89.329)$$

$$\left(\frac{\partial}{\partial t} + \boldsymbol{V} \cdot \boldsymbol{\nabla}\right)V_z = -\frac{1}{\rho}\frac{\partial}{\partial z}\left(P + \frac{B^2}{8\pi}\right) - \frac{\partial \psi}{\partial z}$$

$$+\frac{1}{4\pi\rho}\boldsymbol{B} \cdot \boldsymbol{\nabla}B_z + \frac{1}{\rho}(\boldsymbol{\nabla} \cdot \boldsymbol{\mathcal{T}})_z \qquad (89.330)$$

La même procédure appliquée à l'équation d'induction permet d'obtenir :

$$\left(\frac{\partial}{\partial t} + \boldsymbol{V} \cdot \boldsymbol{\nabla}\right)B_r = \left(\boldsymbol{B} \cdot \boldsymbol{\nabla}\right)V_r - B_r\boldsymbol{\nabla} \cdot \boldsymbol{V} + \eta(\boldsymbol{\Delta B})_r \qquad (89.331)$$

$$\left(\frac{\partial}{\partial t} + \boldsymbol{V} \cdot \boldsymbol{\nabla}\right)B_\phi + \frac{V_\phi B_r}{r} = \left(\boldsymbol{B} \cdot \boldsymbol{\nabla}\right)V_\phi + \frac{B_\phi V_r}{r} - B_\phi\boldsymbol{\nabla} \cdot \boldsymbol{V} + \eta(\boldsymbol{\Delta B})_\phi \qquad (89.332)$$

$$\left(\frac{\partial}{\partial t} + \boldsymbol{V} \cdot \boldsymbol{\nabla}\right)B_z = \left(\boldsymbol{B} \cdot \boldsymbol{\nabla}\right)V_z - B_z\boldsymbol{\nabla} \cdot \boldsymbol{V} + \eta(\boldsymbol{\Delta B})_z \qquad (89.333)$$

§ 90. Approximations

On supposera que l'équilibre du disque est dominé par la force gravitationnelle radiale et la force centrifuge, ce qui permet d'obtenir $(V_\phi)^2/r = \partial\psi/\partial r$. Remarquons que cette hypothèse est cohérente avec les observations de disques montrant à un très bon niveau d'approximation un profil de vitesse Képlerien (Lin & Papaloizou 1996).

Pour développer le système de Hill, on se place à un point de référence situé à un rayon R_0, et associé à une fréquence orbitale $\Omega_0 = V_\phi^0/R_0$. De plus, on utilisera le référentiel tournant avec le point de référence en posant :

$$r' = r \qquad \phi' = \phi - \Omega_0 t \qquad z' = z \qquad (90.334)$$

La vitesse V est alors décomposée sous la forme $\boldsymbol{V} = \boldsymbol{U} + \Omega_0 r\boldsymbol{e_\phi}$, où $\boldsymbol{U}$ peut être interprété comme l'écart à la vitesse képlerienne en R_0, que l'on supposera petite. Par ailleurs, on néglige les effets de courbure, en supposant que les quantités varient sur une échelle $H \ll R_0$ et que l'on se place au voisinage immédiat de R_0, soit $H \sim r - R_0$. A l'ordre le plus élevé en U, on écrit

finalement pour l'équation du mouvement :

$$\left(\frac{\partial}{\partial t'} + \boldsymbol{U} \cdot \boldsymbol{\nabla}\right)U_r - 2\Omega_0 U_\phi = -\frac{1}{\rho}\frac{\partial}{\partial r}\left(P + \frac{B^2}{8\pi}\right) - \frac{\partial \psi}{\partial r} + \Omega_0 r^2$$
$$+ \frac{1}{4\pi\rho}\boldsymbol{B} \cdot \boldsymbol{\nabla}B_r + \frac{1}{\rho}\boldsymbol{\nabla} \cdot \boldsymbol{\mathcal{T}}_r \tag{90.335}$$

$$\left(\frac{\partial}{\partial t'} + \boldsymbol{U} \cdot \boldsymbol{\nabla}\right)U_\phi + 2\Omega_0 U_r = -\frac{1}{\rho r}\frac{\partial}{\partial \phi'}\left(P + \frac{B^2}{8\pi}\right)$$
$$+ \frac{1}{4\pi\rho}\boldsymbol{B} \cdot \boldsymbol{\nabla}B_\phi + \frac{1}{\rho}\boldsymbol{\nabla} \cdot \boldsymbol{\mathcal{T}}_\phi \tag{90.336}$$

$$\left(\frac{\partial}{\partial t'} + \boldsymbol{U} \cdot \boldsymbol{\nabla}\right)U_z = -\frac{1}{\rho}\frac{\partial}{\partial z'}\left(P + \frac{B^2}{8\pi}\right) - \frac{\partial \psi}{\partial z'}$$
$$+ \frac{1}{4\pi\rho}\boldsymbol{B} \cdot \boldsymbol{\nabla}B_z + \frac{1}{\rho}\boldsymbol{\nabla} \cdot \boldsymbol{\mathcal{T}}_z \tag{90.337}$$

et l'équation d'induction :

$$\left(\frac{\partial}{\partial t} + \boldsymbol{U} \cdot \boldsymbol{\nabla}\right)B_r = \left(\boldsymbol{B} \cdot \boldsymbol{\nabla}\right)U_r - B_r \boldsymbol{\nabla} \cdot \boldsymbol{U} + \eta\Delta B_r \tag{90.338}$$

$$\left(\frac{\partial}{\partial t} + \boldsymbol{U} \cdot \boldsymbol{\nabla}\right)B_\phi = \left(\boldsymbol{B} \cdot \boldsymbol{\nabla}\right)U_\phi - B_\phi \boldsymbol{\nabla} \cdot \boldsymbol{U} + \eta\Delta B_\phi \tag{90.339}$$

$$\left(\frac{\partial}{\partial t} + \boldsymbol{U} \cdot \boldsymbol{\nabla}\right)B_z = \left(\boldsymbol{B} \cdot \boldsymbol{\nabla}\right)U_z - B_z \boldsymbol{\nabla} \cdot \boldsymbol{U} + \eta\Delta B_z \tag{90.340}$$

$$\tag{90.341}$$

Le terme de marée $-\partial\psi/\partial r + \Omega_0^2 r$ peut alors être simplifié en considérant l'équilibre radial $\partial\psi/\partial r = r\Omega^2(r)$ et en développant au premier ordre en $R_0 - r$. On obtient alors :

$$-\frac{\partial\psi}{\partial r} + \Omega_0^2 r = -2\Omega_0 R_0(r - R_0)\left(\frac{d\Omega}{dr}\right)_{R_0} \tag{90.342}$$

Pour finir, on reformule le système précédent en considérant que le référentiel est cartésien dans la limite $r - R_0 \ll R_0$. On utilise alors la notation :

$$x = R_0\phi' \qquad y = (r - R_0) \qquad z = -z, \tag{90.343}$$

de façon à se ramener aux notations utilisées en hydrodynamique pour les écoulements de Couette tournants. On obtient finalement le système précédent sous sa forme condensée :

$$\left(\frac{\partial}{\partial t} + \boldsymbol{U} \cdot \boldsymbol{\nabla}\right)\boldsymbol{U} = -\frac{1}{\rho}\boldsymbol{\nabla}\left(P + \frac{B^2}{8\pi}\right) + \frac{1}{4\pi\rho}\boldsymbol{B} \cdot \boldsymbol{\nabla}\boldsymbol{B} + 2\Omega_0 Sy\boldsymbol{e_y}$$
$$-2\boldsymbol{\Omega_0} \times \boldsymbol{U} - \frac{\partial\psi}{\partial z}\boldsymbol{e_z} + \frac{1}{\rho}\boldsymbol{\nabla} \cdot \boldsymbol{\mathcal{T}} \tag{90.344}$$

$$\frac{\partial}{\partial t}\boldsymbol{B} = \boldsymbol{\nabla} \times (\boldsymbol{U} \times \boldsymbol{B}) + \eta\Delta\boldsymbol{B} \tag{90.345}$$

où l'on a noté $S = -(rd\Omega/dr)_{R_0}$ le cisaillement moyen de l'écoulement laminaire $U_x = Sy$, solution des équations précédentes. Dans le cas incompressible, on pourra écrire $\boldsymbol{\nabla} \cdot \boldsymbol{V} = 0$ de sorte que le terme de viscosité se simplifie sous la forme $1/\rho\boldsymbol{\nabla} \cdot \boldsymbol{\mathcal{T}} = \nu\Delta\boldsymbol{V}$ où on définira la viscosité cinématique $\nu = \eta_v/\rho$.

B

Quelques formules d'intégration numérique

Les formules présentées ici sont tirées de Press *et al.* (2002), Brandenburg (2003) et Canuto *et al.* (1988). Elles sont données dans ce manuscrit afin d'avoir une base complète et pratique pour étudier les schémas aux différences finis. On pourra néanmoins se reporter aux références proposées pour plus de détails sur la dérivation de ces formules.

1. Formules aux différences finies

§ 91. Formules centrées

Je présente ici les formules différences finies centrées, respectivement d'ordre 2, 4, 6, 8 et 10, et en considérant un pas de grille égal à δ_x. On obtient :

$$f'_i = (-f_{i-1} + f_{i+1})/(2\delta x) \tag{91.346}$$

$$f'_i = (f_{i-2} - 8f_{i-1} + 8f_{i+1} - f_{i+2})/(12\delta x) \tag{91.347}$$

$$f'_i = (-f_{i-3} + 9f_{i-2} - 45f_{i-1} + 45f_{i+1} - 9f_{i+2} + f_{i+3})/(60\delta x) \tag{91.348}$$

$$f'_i = (3f_{i-4} - 32f_{i-3} + 168f_{i-2} - 672f_{i-1} \tag{91.349}$$
$$+672f_{i+1} - 168f_{i+2} + 32f_{i+3} - 3f_{i+4}/(840\delta x)$$

$$f'_i = (-2f_{i-5} + 25f_{i-4} - 150f_{i-3} + 600f_{i-2} - 2100f_{i-1} \tag{91.350}$$
$$+2100f_{i+1} - \dots)/(2520\delta x)$$

pour les dérivées premières et :

$$f_i'' = (f_{i-1} - 2f_i + f_{i+1})/(\delta x^2) \tag{91.351}$$

$$f_i'' = (-f_{i-2} + 16f_{i-1} - 30f_i + 16f_{i+1} - f_{i+2})/(12\delta_x^2) \tag{91.352}$$

$$f_i'' = (2f_{i-3} - 27f_{i-2} + 270f_{i-1} - 490f_i + 270f_{i+1} - 27f_{i+2} + 2f_{i+3})/(180\delta_x^2) \tag{91.353}$$

$$f_i'' = (-9f_{i-4} + 128f_{i-3} - 1008f_{i-2} + 8064f_{i-1} - 14350f_i \tag{91.354}$$
$$+ 8064f_{i+1} - \dots)/(5040\delta_x^2)$$

$$f_i'' = (8f_{i-5} - 125f_{i-4} + 1000f_{i-3} - 6000f_{i-2} + 42000f_{i-1} - 73766f_i \tag{91.355}$$
$$+ 42000f_{i+1} - \dots)/(25200\delta_x^2)$$

pour les dérivées secondes.

§ 92. Formules upwind

Les formules upwind sont particulièrement utiles dans les équations d'advection, car elle permettent de dissiper les oscillations parasites qui peuvent apparaître au voisinage des forts gradients de vitesse ou de densité. Elles sont données ici pour le schéma d'advection lorsque la vitesse est positive. On retrouvera facilement leurs expressions lorsque la vitesse est négative par symétrie. Les formules données ci-après sont d'ordre respectif 1, 3, 4 et 6.

$$f_i' = (-f_{i-1} + f_i)/\delta_x \tag{92.356}$$

$$f_i' = (2f_{i-2} - 12f_{i-1} + 6f_i + 4f_{i+1})/(12\delta_x) \tag{92.357}$$

$$f_i' = (-f_{i-3} + 6f_{i-2} - 18f_{i-1} + 10f_i + 3f_{i+1})/(12\delta_x) \tag{92.358}$$

$$f_i' = (f_{i-4} - 8f_{i-3} + 30f_{i-2} - 80f_{i-1} + 35f_i + 24f_{i+1} - 2f_{i+2})/(60\delta_x) \tag{92.359}$$

2. Algorithme de Runge-Kutta

On pourra trouver dans Press *et al.* (2002) une méthode de calcul générale de l'algorithme de Runge-Kutta. Retenons simplement que ce type de schéma explicite en temps permet d'obtenir une précision d'intégration d'ordre arbitrairement élevé. En pratique, on s'arrête souvent à l'ordre 4. Pour une équation différentielle du type :

$$\frac{d\psi}{dt} = \Delta(t, \psi), \tag{92.360}$$

les deux algorithmes de Runge-Kutta les plus connus s'écrivent :

- Schéma Runge-Kutta d'ordre 2

$$k1_i = \delta t \Delta(t, \psi_i^n)$$
$$k2_i = \delta t \Delta(t + \frac{\delta t}{2}, \psi_i^n + \frac{1}{2}k1_i)$$
$$\psi_i^{n+1} = \psi_i^n + k2_i$$

- Schéma Runge-Kutta d'ordre 4

$$
\begin{aligned}
k1_i &= \delta t \Delta(t, \psi_i^n) \\
k2_i &= \delta t \Delta(t + \frac{\delta t}{2}, \psi_i^n + \frac{1}{2} k1_i) \\
k3_i &= \delta t \Delta(t + \frac{\delta t}{2}, \psi_i^n + \frac{1}{2} k2_i) \\
k4_i &= \delta t \Delta(t + \delta t, \psi_i^n + k3_i) \\
\psi_i^{n+1} &= \psi_i^{n+1} + \frac{1}{6} k1_i + \frac{1}{3} k2_i + \frac{1}{3} k3_i + \frac{1}{6} k4_i
\end{aligned}
$$

C

Relation de dispersion des modes exponentielles de la SRI.

§ 93. Dérivation de la relation de dispersion

En utilisant les hypothèses de raccordement présentées au § 63.1, on écrit les conditions aux limites devant être vérifiées par les solutions (63.236) et (63.237). Comme le milieu (1) s'étend jusqu'à $-\infty$, on choisit les solutions du milieu (1) s'annulant pour $y \rightarrow \infty$ (hypothèse de raccordement asymptotique). En supposant que $k_{F_1} > 0$, on obtient alors la condition $A_1^- = 0$. Un raisonnement similaire dans le milieu (3) mène à la condition $A_3^+ = 0$. Les conditions aux limites (62.230),(62.231), (62.234) et (62.235) permettent alors d'écrire le système d'équations :

$$0 = A_1^+ \rho_1 \exp\left(-k_{F_1}L/2\right) - A_2^+ \rho_2 \exp\left(-k_{F_2}L/2\right) - A_2^- \rho_2 \exp\left(k_{F_2}L/2\right) \quad (93.361)$$

$$0 = A_2^+ \rho_2 \exp\left(k_{F_2}L/2\right) + A_2^- \rho_2 \exp\left(-k_{F_2}L/2\right) - A_3^- \rho_1 \exp\left(-k_{F_1}L/2\right) \quad (93.362)$$

$$0 = A_1^+ \left(\omega_c \alpha + k_{F_1}(\omega + \omega_s)\right) \exp\left(-k_{F_1}L/2\right) \quad (93.363)$$
$$- A_2^+ \left(\omega_c \alpha + k_{F_2}(\omega + \omega_s)\right) \exp\left(-k_{F_2}L/2\right)$$
$$- A_2^- \left(\omega_c \alpha - k_{F_2}(\omega + \omega_s)\right) \exp\left(k_{F_2}L/2\right)$$

$$0 = A_2^+ \left(\omega_c \alpha + k_{F_2}(\omega - \omega_s)\right) \exp\left(k_{F_2}L/2\right) \quad (93.364)$$
$$+ A_2^- \left(\omega_c \alpha - k_{F_2}(\omega - \omega_s)\right) \exp\left(-k_{F_2}L/2\right)$$
$$- A_3^- \left(\omega_c \alpha - k_{F_1}(\omega - \omega_s)\right) \exp\left(-k_{F_1}L/2\right)$$

Où l'on a posé $\omega_c = 2\Omega$ et $\omega_s = SL\alpha/2$. On trouve alors une solution non triviale au système linéaire précédent en annulant le déterminant correspondant. On obtient ainsi après un peu

d'algèbre :

$$\left(\omega_s^2 - \omega^2\right)\left(s^2 \exp(k_{F_2}L) - d^2 \exp(-k_{F_2}L)\right) \tag{93.365}$$
$$-2\delta\alpha\omega_c\omega_s\left(s \exp(k_{F_2}L) - d \exp(-k_{F_2}L)\right)$$
$$+2\omega_c^2\alpha^2\delta^2 \sinh(k_{F_2}L) \;\; = \;\; 0$$

avec $d = k_{F_1}\rho_2 - k_{F_2}\rho_1$; $s = k_{F_1}\rho_2 + k_{F_2}\rho_1$ et $\delta = \rho_1 - \rho_2$. De plus, il faut appliquer les conditions sur les profils d'équilibre hydrostatiques (Eqns. 62.228 et 62.229). Par simplicité, je supposerai des profils isothermes, ce qui permet d'écrire la fréquence de Brunt-Väisälä sous la forme :

$$N_i^2 = \frac{(\gamma - 1)g^2\rho_i}{\gamma P_i}. \tag{93.366}$$

Ainsi, en utilisant les conditions aux limites (62.228)-(62.229) sur les vecteurs d'onde de Froude, on obtient finalement :

$$k_{F_1} = \sqrt{\frac{\rho_2}{\rho_1}}k_{F_2} \tag{93.367}$$

On peut alors simplifier la relation de dispersion (93.365) en utilisant un seul paramètre $r = (\rho_2/\rho_1)^{3/2}$, reflétant les caractéristiques différentes des milieux (1) et (2) :

$$\omega^2 \;\; = \;\; \omega_s^2 \tag{93.368}$$
$$- \;\; \frac{2(1 - r^{2/3})}{k_{F_2}G}\alpha\omega_c\omega_s\left(r \sinh(k_{F_2}L) + \cosh(k_{F_2}L)\right)$$
$$+ \;\; \frac{\omega_c^2\alpha^2\left(1 - r^{2/3}\right)^2}{k_{F_2}^2 G} \sinh(k_{F_2}L)$$

D
Publications

Plan du chapitre

1. On the relevance of subcritical hydrodynamic turbulence to accretion disk transport

**Astronomy
&
Astrophysics**

On the relevance of subcritical hydrodynamic turbulence to accretion disk transport

G. Lesur and P.-Y. Longaretti

Laboratoire d'Astrophysique, Observatoire de Grenoble, BP 53, 38041 Grenoble Cedex 9, France
e-mail: [geoffroy.lesur;pierre-yves.longaretti]@obs.ujf-grenoble.fr

ABSTRACT

Hydrodynamic unstratified Keplerian flows are known to be linearly stable at all Reynolds numbers, but may nevertheless become turbulent through nonlinear mechanisms. However, in the last ten years, conflicting points of view have appeared on this issue. We have revisited the problem through numerical simulations in the shearing sheet limit. It turns out that the effect of the Coriolis force in stabilizing the flow depends on whether the flow is cyclonic (cooperating shear and rotation vorticities) or anticyclonic (competing shear and rotation vorticities); Keplerian flows are anticyclonic. We have obtained the following results:

i/ The Coriolis force does not quench turbulence in subcritical flows; however, turbulence is more efficient, and much more easily found, in cyclonic flows than in anticyclonic ones.

ii/ The Reynolds number/rotation/resolution relation has been quantified in this problem. In particular we find that the resolution demand, when moving away from the marginal stability boundary, is much more severe for anticyclonic flows than for cyclonic ones. Presently available computer resources do not allow numerical codes to reach the Keplerian regime.

iii/ The efficiency of turbulent transport is directly correlated to the Reynolds number of transition to turbulence Rg, in such a way that the Shakura-Sunyaev parameter $\alpha \sim 1/Rg$. This correlation is nearly independent of the flow cyclonicity. The correlation is expected on the basis of generic physical arguments.

iv/ Even the most optimistic extrapolations of our numerical data show that subcritical turbulent transport would be too inefficient in Keplerian flows by several orders of magnitude for astrophysical purposes. Vertical boundary conditions may play a role in this issue although no significant effect was found in our preliminary tests.

v/ Our results suggest that the data obtained for Keplerian-like flows in a Taylor-Couette settings are largely affected by secondary flows, such as Ekman circulation.

Key words. accretion, accretion disks – hydrodynamics – instabilities – turbulence

1. Introduction

The question of the existence and physical origin of turbulence in accretion disks has been lively debated for a number of decades. Generally speaking, there are a priori two basic ways in which an accretion disk can become turbulent. In the first way, some linear instability is present in the flow, and its nonlinear development eventually drives turbulence. In the second one, the flow is linearly stable, and undergoes a direct laminar-turbulent transition once a certain threshold in Reynolds number is reached. The first type of transition to turbulence is called supercritical, and the second, (globally) subcritical.

Global instabilities (such as the Papaloizou & Pringle 1984 instability) seem unpromising to drive turbulence (Blaes 1987; Hawley 1991). As for local instabilities, an astrophysically important example of supercritical transition is provided by the magneto-rotational instability (MRI) which has been extensively studied following the pioneering work of Balbus, Hawley and their collaborators (Balbus & Hawley 1991; Hawley et al. 1995; see Balbus 2003, for a recent review). The turbulent transport induced by this instability is by now characterized in a number of instances, and has been called upon even when only some fraction of the disk is ionized, as in the midplane region of YSOs inner disks – the dead-zone (Gammie 1996; Fleming & Stone 2003). However, the reduced efficiency of the transport in this case, as well as the possible existence of disks which may not support MHD phenomena at all, has prompted some upsurge of interest in purely hydrodynamic instabilities. A local, baroclinic-like instability has been observed in global simulations by Klahr & Bodenheimer (2003). Local stability analyzes (Klahr 2004; Johnson & Gammie 2005a) find transient instability in this context, but shearing box simulations indicate that this does not drive turbulence (Johnson & Gammie 2005b). Urpin (2003) discusses an instability related

to vertical shear and heat transport of the Goldreich-Schubert type (Goldreich & Schubert 1967); however, this instability produces only a rather weak radial transport (Arlt & Urpin 2004). More recently, Dubrulle et al. (2005b) and Shalybkov & Ruediger (2005) have discussed an instability arising when both the fluid differential rotation and vertical stratification are stabilizing according to the Høiland criterion. However, it seems that this instability is connected to the presence of walls, and is dynamically important only when the inter-wall distance is small enough for a resonant-like interaction to take place[1] (Satomura 1981), otherwise disturbances are confined to the near boundary zone; a related result has recently been found in the astrophysics literature (Umurhan 2005). Earlier analytic and numerical investigations have shown this instability to be absent in local disk models (Goodman & Balbus 2001; Brandenburg & Dintrans 2001; Rüdiger et al. 2002). Note finally that vertical convection in a stratified disk can in principle also drive turbulence; however, it induces inwards transport instead of the required outwards one (Cabot 1996; Stone & Balbus 1996). Therefore, no local instability has yet been found in the hydrodynamic regime, which would explain the turbulent transport taking place in accretion disks.

Subcritical transition to turbulence is the subject of the present work. The non-rotating plane Couette flow provides a classical (and to date the best understood) example of a system undergoing a subcritical transition. Although the nature and mechanism of the transition remained elusive for decades, it has been identified in the recent years, in laboratory experiments (Daviaud et al. 1992; Dauchot & Daviaud 1995a,b; Bottin et al. 1997), numerical simulations (Hamilton et al. 1995; see also Schmiegel & Eckhardt 1997 and Eckhardt & Mersmann 1999), and theoretical analyzes (in particular Waleffe 1997; Waleffe 2003). Earlier investigations of the problem have focused on the role of nonlinear instabilities in subcritical shear flows, based on Landau-like toy-models on the one hand (e.g., Drazin & Reid 1981 and references therein), and analysis of the linear stability of finite amplitude defects in the flow profile on the other (Lerner & Knobloch 1988; Dubrulle & Zahn 1991; Dubrulle 1993); unfortunately, such analyzes yield little information on the existence and location of the turbulent state in parameter space and on the turbulent transport efficiency, unless further ad hoc assumptions are made.

In any case, on the basis of the empirically observed subcritical transition in laboratory flows, it was suggested that a similar process is relevant in accretion disks (Shakura et al. 1978), in spite of their very different prevailing physical conditions. This suggestion was tested and challenged in a series of numerical simulations performed by Balbus et al. (1996) and Hawley et al. (1999), in the shearing sheet limit. Transition to turbulence was not found in these simulations for Keplerian-like flows. The simulations were performed with two different finite difference codes (a PPM type code, and the ZEUS code), up to a resolution of 256^3. These two works concluded that a stabilizing Coriolis force prevents the existence of turbulence

in the simulated flows, except in the immediate vicinity of the linear marginal stability limits.

This conclusion was in turn questioned by Richard & Zahn (1999), on the basis of the Taylor-Couette experiments performed by Wendt (1933) and Taylor (1936). These experimental results display a subcritical transition to turbulence in presence of a stabilizing Coriolis force. Also, new sets of experiments have been carried out in order to bring the experimental conditions closer to the ones prevailing in a Keplerian flow. Namely, a Taylor-Couette apparatus was used in conditions of radially decreasing angular velocity and radially increasing specific angular momentum. Turbulence was again found for high enough Reynolds numbers (Richard 2001; Richard et al. 2001) but the results are not unambiguous, as the potential role of secondary flows induced by the boundary conditions in the experiments, such as Ekmann's circulation, is unclear, in spite of the attention devoted to this point in the experiments. In any case, a subcritical transition is also found in all experiments of shear flows on which a linearly stabilizing Coriolis force is superimposed (Longaretti & Dauchot 2005).

Longaretti (2002) has argued from a phenomenological analysis that the lack of turbulence in the simulations performed to date was due to a lack of resolution, as the Coriolis force may increase the range of scales that need to be resolved for a subcritical turbulent transition to show up. On the other hand, on the basis of a newly developed Reynolds stress closure scheme (Ogilvie 2003), Garaud & Ogilvie (2005) find that Keplerian flows may or may not be turbulent depending on the parameters of the scheme. For their favored choice of parameters, unbounded Keplerian flows are not turbulent, on the contrary to linearly stable, wall-bounded Taylor-Couette flows.

The recent astrophysical literature on the problem of subcritical transition has also focused on the concept of transient growth in Keplerian flows (Chagelishvili et al. 2003; Tevzadze et al. 2003; Yecko 2004; Umurhan & Regev 2004; Mukhopadhyay et al. 2005; Afshordi et al. 2005). Due to the nonnormal character of the Navier-Stokes equation, linear modes can transiently be strongly amplified in shear flows, although on the long run they must viscously decay. It has been argued that this transient growth can be relevant to astrophysical disks in two different ways. First, 3D turbulence (or an external forcing) can couple to large scale 2D structures; the (statistical) amplitude of these structures can be large, under the combined action of this coupling, of transient growth and of viscous decay, and these 2D structures may contribute to the overall transport in the disk (Ioannou & Kakouris 2001). Secondly, a large transient growth has been invoked in the bypass scenario of transition to turbulence, which involves an interplay between nonnormality and nonlinearity (see, e.g., Grossman 2000; Brosa & Grossmann 1999). Waleffe (1995) has emphasized the key role played by nonlinear interactions in the context of the recently identified turbulent self-sustaining process of non-rotating plane Couette flows (Hamilton et al. 1995; Waleffe 1997). Even though transient growth explains the strong modulations of the streamwise velocity from relatively weak streamwise rolls involved in this self-sustaining mechanism, the existence and properties of the turbulent basin of attraction for the full nonlinear dynamics are

---

[1] We thank Stéphane Le Dizes for bringing this point to our attention.

apparently poorly constrained by the nonnormal linear problem characteristics.

Our present understanding of the possible existence of a dynamically significant subcritical turbulent transition in accretion disks is unsatisfying in several respects, calling for a reinvestigation of the problem. On the one hand, the relevance of the available laboratory experiments to accretion disk turbulence is at best unclear, as will be shown in the course of the present work (for a different opinion, see Hersant et al. 2005). On the other hand, the absence of subcritical turbulence in the shearing sheet local model of accretion disks used by Balbus et al. (1996) and Hawley et al. (1999) may be an effect of various numerical limitations, namely, algorithm choice, limited resolution, nature of the boundary conditions, imposed aspect ratio and initial conditions of the simulations. Of these options, only the first two have been partially addressed in these previous investigations, leading to questions concerning the "effective Reynolds number" of the performed simulations – an ill-defined process-dependent concept, that we shall clarify in the context of the present problem. Following the suggestion of Longaretti (2002), the primary aim of the present work is to investigate in a more systematic way, through numerical simulations of plane parallel, rotating shear flows, the effects of finite resolution on the results. The effects of the other factors listed above are also somewhat explored, but to a lesser extent. Both cyclonic and anticyclonic rotation are considered; although cyclonic rotation is not relevant to accretion disks, it turns out that cyclonic flows behave very differently from anticyclonic ones, opening some interesting perspective into the nature of the problem.

This paper is organized as follows. Section 2.1 collects the background material relevant to the problem. First, the form of the equations solved is provided, and the global energy budget recalled, before discussing linear stability limits. The section is concluded by a summary of the effect of a stabilizing rotation in shear flows as characterized by the available laboratory experiments. The next section presents the various codes used in this work, and the numerical results obtained with them. Section 4 discusses various aspects of our numerical results, most notably the role of resolution and boundary conditions on the numerical side, the role of the Coriolis force, the underlying phenomenological picture, and the astrophysical implications, on the physical side. A summary is provided in Sect. 5, along with an outlook on the question of turbulence in accretion disks.

2. Rotating plane shear flows: a summary

The present investigation is concerned with the nonlinear instability of laminar flows characterized by a uniform shear, in the presence of a uniform global rotation. The direction of the flow is identified with the x axis (streamwise direction), and the direction of the shear with the y axis (shearwise direction); rotation is applied along the z axis (spanwise direction). The laminar flow $\boldsymbol{u}_L$ is invariant in the streamwise and spanwise directions (in particular, the vertical stratification expected in a real disk is ignored): $\boldsymbol{u}_L = U(y)\boldsymbol{e}_x$.

Such a flow can be used to numerically model either a local portion of an accretion disk, or experiments on rotating plane
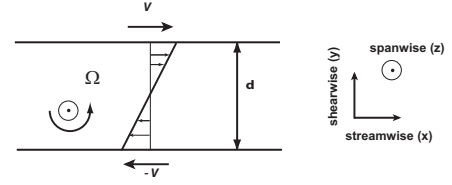

Fig. 1. Sketch of the configuration of rotating plane shear flows.

Couette flows, depending on the nature of the applied boundary condition in the shearwise direction (in practice, either rigid or shearing sheet; see next section). The configuration is represented in Fig. 1.

2.1. Equations of motion

The most useful form of the Navier-Stokes equation, for our present purpose, is obtained by separating the laminar flow $\boldsymbol{u}_L$ and the deviation from laminar $\boldsymbol{w}$ in the total velocity $\boldsymbol{u}$ in the rotating frame, leading to

$$\frac{\partial \boldsymbol{w}}{\partial t} + \boldsymbol{w} \cdot \boldsymbol{\nabla} \boldsymbol{w} = S \cdot y \frac{\partial \boldsymbol{w}}{\partial x} + (2\Omega + S)w_y\boldsymbol{e}_x - 2\Omega w_x\boldsymbol{e}_y$$
$$- \frac{\boldsymbol{\nabla}\delta\pi}{\rho} + \nu\Delta\boldsymbol{w}, \tag{1}$$

where the gradient terms balancing the laminar flow Coriolis force has been subtracted out to form the effective generalized pressure $\delta\pi$ (which therefore absorbs the equilibrium centrifugal, gravitational and/or pressure force term, depending on the considered equilibrium problem); Ω is the flow rotation velocity in an inertial frame, and $S = -\mathrm{d}U/\mathrm{d}y$ is the shear. The convention adopted here is that the sign of S is chosen to be positive when the flow is cyclonic, i.e., when the contributions of shear and rotation to the flow vorticity have the same sign. With our choice of axes, this implies that $S = -2S_{xy}$, where $S_{ij} = 1/2(\partial_i u_{L,j} + \partial_j u_{L,i})$ is the usual deformation tensor. The system is closed either with the usual continuity equation supplemented by a polytropic equation of state, or, for simplicity, through an incompressibility assumption ($\boldsymbol{\nabla} \cdot \boldsymbol{w} = 0$).

The relevant global time-scales of the problem are the shear time-scale $t_s = |S^{-1}|$, the viscous one $t_\nu = d^2/\nu$ (d is the gap in the experiment, or the shearwise size of the shearing sheet box), and the rotation time-scale related to the Coriolis force $t_\Omega = (2\Omega)^{-1}$; they relate to the advection term, the viscous term, and the Coriolis force term, respectively. Correlatively, the flow is described by two dimensionless numbers, the Reynolds number

$$\mathrm{Re} = t_\nu/t_s = |S|d^2/\nu, \tag{2}$$

and the rotation number

$$R_\Omega = \mathrm{sgn}(S)t_s/t_\Omega = 2\Omega/S. \tag{3}$$

For Keplerian flows, $R_\Omega = -4/3$. More generally, if one assumes that the large scale rotation of an astrophysical disk follows a power-law, $\Omega(r) \propto r^{-q}$, one locally has $R_\Omega = -2/q$ in the disk.

28   G. Lesur and P.-Y. Longaretti: Subcritical turbulence in rotating shear flows

Note that our Reynolds number is defined on the outer scales, and not on the turbulent ones, such as, e.g., the Taylor microscale. Large values ($\sim 10^4$) of this number are involved in the problem investigated here; the correlative numerical requirements are discussed in Sect. 4.4.

2.2. Energy budget

As the global energy budget plays some role in the discussion of the results, it is rederived here. In the following equations, the bracket notation refers to a volume average of the bracketed quantity. The averaging volume is the simulation one, and shearing-sheet boundary conditions are assumed in the derivation, for definiteness. For the kinetic energy in the streamwise and shearwise directions, one finds:

$$\frac{\partial}{\partial t}\left\langle\frac{w_x^2}{2}\right\rangle = S\,(R_\Omega + 1)\,\langle w_x w_y\rangle$$
$$-\left\langle\frac{w_y}{\rho}\frac{\partial\delta\pi}{\partial x}\right\rangle + \nu\langle w_x\Delta w_x\rangle, \tag{4}$$

$$\frac{\partial}{\partial t}\left\langle\frac{w_y^2}{2}\right\rangle = -S\,R_\Omega\,\langle w_x w_y\rangle$$
$$-\left\langle\frac{w_y}{\rho}\frac{\partial\delta\pi}{\partial y}\right\rangle + \nu\langle w_y\Delta w_y\rangle. \tag{5}$$

Instead of the vertical equation, it is more instructive to write down the total kinetic energy equation:

$$\frac{\partial}{\partial t}\left\langle\frac{\boldsymbol{w}^2}{2}\right\rangle = S\,\langle w_x w_y\rangle - \epsilon, \tag{6}$$

where

$$\epsilon = \nu\sum_i\langle(\boldsymbol{\nabla} w_i)^2\rangle \tag{7}$$

is the usual energy injection rate of turbulence cascade arguments[2]. In this last equation the incompressibility condition and the boundary conditions have been used in the reexpression of the pressure term, and an integration by part has been performed on the viscous term (a constant kinematic viscosity ν is assumed).

In statistical steady-state, Eq. (6) reduces to,

$$S\,\langle w_x w_y\rangle = \epsilon. \tag{8}$$

As pointed out by Balbus et al. (1996), the fact that $\epsilon > 0$ implies that in steady state, the shear rate and the Reynolds stress responsible for radial transport have identical signs. This result has a direct physical interpretation: the imposed shear prevents the flow to be in global thermodynamic equilibrium. Nevertheless, the flow tries to restore this global equilibrium by radially transporting momentum through the turbulent Reynolds stress from regions of larger momentum to regions of lower momentum, consistently with Eq. (8).

Note finally that, in Eqs. (4) and (5), the pressure-velocity correlation terms *cannot* be neglected, as they are of the order of the cascade energy injection term ϵ. This is almost unavoidable, as pressure is the only force that can provide for the acceleration of fluid particles in turbulent motions. As a matter of fact, the energy budget of any particular velocity component depends critically on the behavior of the velocity-pressure correlations, which are notoriously difficult to model (Speziale 1991). Ignoring this term in the analysis of the energetics therefore leads to dubious or erroneous conclusions.

2.3. Linear stability limits

Surprisingly enough, the question of the linear stability limits of the simple rotating shear flows considered here is not completely solved to date. Focusing for the time being on purely streamwise-independent perturbations, instability with respect to local perturbations follows when (Pedley 1969; Leblanc & Cambon 1997; Sipp & Jacquin 2000)

$$R_\Omega(R_\Omega + 1) < 0, \tag{9}$$

or, equivalently, $-1 < R_\Omega < 0$.

In plane Couette flows, it has been proven that $R_\Omega^+ \equiv 0$ is the correct cyclonic marginal stability limit for non streamwise-invariant perturbations as well, at all Reynolds numbers (Romanov 1973). No such generic proof exists at the anticyclonic marginal stability limit ($R_\Omega^- \equiv -1$). However, various linear and nonlinear numerical investigations suggest that this is indeed the case (Cambon et al. 1994; Komminaho et al. 1996; Bech & Andersson 1997). These results belong to plane Couette flows with rigid boundary conditions in the shearwise direction, but tend to prove that a local criterion captures the correct stability limit, as observed, e.g., in the simulations of Balbus et al. (1996) and Hawley et al. (1999).

The physics behind Eq. (9) can be captured by a displaced particle argument (Tritton & Davies 1981; Tritton 1992). This argument is reproduced in Appendix A for the reader's convenience. Note that Eq. (9) is identical to Rayleigh's specific angular momentum criterion for the centrifugal instability, as the usual epicyclic frequency reads $\kappa^2 = S^2 R_\Omega(1 + R_\Omega)$. However, in the plane shear flow limit of cylindrical flows, the concept of specific angular momentum used in the derivation of Rayleigh's criterion no longer has meaning, so that one must follow a different route, as done here. Note also that, consequently, the Rayleigh criterion for the centrifugal instability in the inertial frame can also be understood from the action of the Coriolis force in the rotating frame (a somewhat surprising, although not new conclusion), as the displaced particle argument of Appendix A is readily extended to cylindrical flows.

2.4. Subcritical transition in rotating plane Couette flows: a summary of relevant experimental results

In the laboratory, non-rotating plane Couette flows undergo a subcritical transition to turbulence at Re $\simeq 1500$. The transition Reynolds number steeply increases if a stabilizing rotation and/or a curvature is superimposed on the flow. The conceptually cleanest way to add rotation to a plane Couette flow is

---

[2] Because the rate of energy transfer in scale is constant in a Kolmogorov-like argument, the injection rate is directly related to the small-scale dissipation rate.

to place a plane Couette apparatus on a rotating table. Also, by considering a Taylor-Couette apparatus with varying gap width and independently rotating cylinders, one obtains a flow in which both rotation and curvature effects can be studied, and which reduces to a rotating plane Couette flow in the narrow gap limit. For a more complete discussion of the distinction and characterization of rotation and curvature in Taylor-Couette experiments, and of the related experimental data, the reader is referred to Longaretti & Dauchot (2005).

For the range of parameters studied to date in the experiments, it turns out that rotation and curvature effects on the transition Reynolds number are superposed in an mostly additive way, so that both plane Couette flows and Taylor-Couette flows can in principle be used to characterize the effect of rotation. Concerning cyclonic flows, the only directly relevant data have been collected by Tillmark & Alfredsson (1996) with the help of a plane Couette flow apparatus placed on a rotating table. For anticyclonic flows, the only available experiments are those of Richard and coworkers (Richard 2001; Richard et al. 2001), who used a Taylor-Couette apparatus. The range of rotation number R_Ω explored in these experiments is 0 to 0.1 for cyclonic rotation, and -1.6 to -1 for anticyclonic rotation. The data are shown in Fig. 2

The important point to note here is the steep dependence of the transition Reynolds number with the "distance" to marginal stability, with a typical slope $|\Delta R_g|/|\Delta R_\Omega| \sim 10^4 - 10^5$.

3. Numerical codes, strategy, and results

In the present work, we are concerned with rotating, unstratified uniform shear flows. Periodic boundary conditions hold in the direction of the flow (x axis) and the "vertical" direction (z axis), and either shearing sheet or rigid boundary conditions are applied in the direction of the shear (y direction). The vertical axis is also the axis of rotation of the flow. The shearing sheet boundary conditions are described in detail by Hawley et al. (1995). Shearing sheet flows thus modelled can be viewed as a local approximation of disk flows, while the use of mixed rigid-periodic boundary conditions is appropriate to numerically represent the rotating plane Couette flows of laboratory experiments, as routinely done in the fluid mechanics community.

3.1. Numerical codes

Two different 3D codes have been written for the present work: a finite difference compressible code, similar to ZEUS (Stone & Norman 1992), but restricted to the Cartesian geometry, and rigid-periodic or shearing sheet boundary conditions; and a 3D incompressible Fourier code, in Cartesian geometry, and implementing only the shearing sheet boundary conditions. An explicit kinematic viscosity term is added in both codes, upon which the Reynolds number is defined. Both codes were parallelized using the Message Passing Interface.

The shearing sheet boundary conditions induce some changes with respect to a standard Fourier code. As a matter of fact, while we were developing this code, the work by Umurhan & Regev (2004) appeared, which implements the
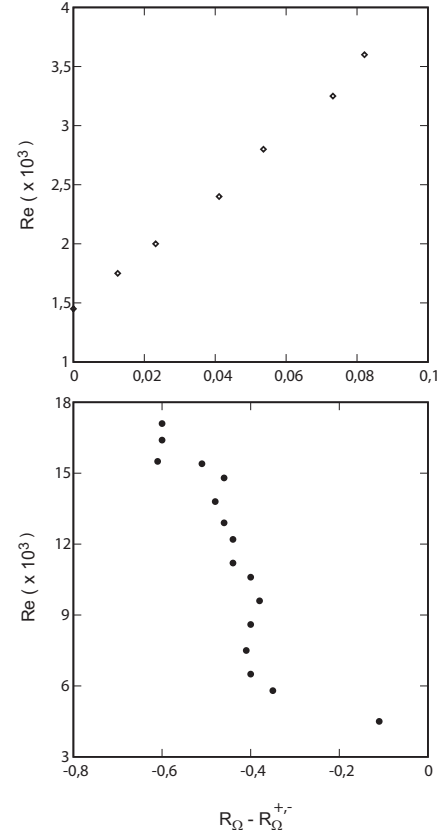
Fig. 2. Data on the Reynolds number of subcritical transition to turbulence as a function of the rotation number R_Ω, measured from the appropriate marginal stability limit $R_\Omega^\pm$ (see text). *Top panel*: cyclonic plane Couette flow (data from Tillmark & Alfredsson 1996). *Bottom panel*: anticyclonic Taylor-Couette flow (data from Richard 2001). The anticyclonic data are more difficult to collect, and consequently noisier.

same technique. Therefore, our description of the required changes will be brief, and we refer the reader to this recent paper for details.

To get effective periodic boundary conditions on the 3 axes, one needs to write Eq. (1) in the sheared frame defined by:

$$t' = t \tag{10}$$
$$x' = x + S \cdot y \cdot t \tag{11}$$
$$y' = y \tag{12}$$
$$z' = z. \tag{13}$$

In this shearing frame, Eq. (1) (supplemented by the incompressibility condition) becomes:

$$\frac{\partial \boldsymbol{w}}{\partial t'} + \boldsymbol{w} \cdot \tilde{\boldsymbol{\nabla}} \boldsymbol{w} = -\frac{\tilde{\boldsymbol{\nabla}} \delta \pi}{\rho} - 2\Omega\, w_x \boldsymbol{e_y} + (2\Omega + S) w_y \boldsymbol{e_x}$$
$$+ \nu \tilde{\Delta} \boldsymbol{w} \tag{14}$$
$$\tilde{\boldsymbol{\nabla}} \cdot \boldsymbol{w} = 0 \tag{15}$$

in which $\tilde{\boldsymbol{\nabla}} = \partial_{x'} \boldsymbol{e_{x'}} + (\partial_{y'} - S t' \partial_{x'}) \boldsymbol{e_{y'}} + \partial_{z'} \boldsymbol{e_{z'}}$ and $\tilde{\Delta} = \tilde{\boldsymbol{\nabla}} \cdot \tilde{\boldsymbol{\nabla}}$.

Since the shearing box is a periodic box in the shearing frame, this last formulation of the Navier-Stokes equation can be written in 3D-Fourier Space. Defining:

$$\boldsymbol{\mu} = \boldsymbol{k} - S\,t k_x \boldsymbol{e_y}, \tag{16}$$

one finally obtains:

$$\frac{\partial \hat{\boldsymbol{w}}}{\partial t'} + i\boldsymbol{\mu} \cdot \widehat{\boldsymbol{w} \otimes \boldsymbol{w}} = -i\boldsymbol{\mu}\frac{\widehat{\delta\pi}}{\rho} - 2\Omega\,\hat{w}_x \boldsymbol{e_y} + (2\Omega + S)\hat{w}_y \boldsymbol{e_x}$$
$$-\nu\mu^2\boldsymbol{w} \tag{17}$$
$$\boldsymbol{\mu} \cdot \hat{\boldsymbol{w}} = 0. \tag{18}$$

These are the equations actually used in our spectral code. The nonlinear term is computed using the 2/3 dealiasing rule with a pseudo-spectral method (see e.g. Peyret 2002 for a description of this point) and each time-step is evaluated using a 4th order Runge Kutta Scheme. One should note that a k-wave in the sheared frame actually appears as a $\mu(t)$-wave in the steady frame. Then, as time goes on in the simulation, the k-grid describes higher spatial frequency in the steady frame and consequently, the large scales are not computed anymore. Since nonlinear coupling limits the shearing of any wave-number, a remap procedure is periodically applied all along the simulation, and prevents to loose information on the large scale[3] (Rogallo 1981). This kind of algorithm has been extensively described by Umurhan & Regev (2004) using a 2D spectral code and the reader should refer to this publication for technical details on the remap procedure.

The choice of these two codes was made first for purposes of comparison with previous work, and secondly to allow us to cross-check the potential limitations of one code against the other; e.g., the shearing sheet boundary conditions and sheared spatial basis Eq. (16) have their own limitations, as the sheared basis forms a complete basis for shearing sheet boundary conditions, but only for these conditions.

The three codes were tested in a variety of ways. The first test was to reproduce the non-rotating plane Couette flow behavior computed by Hamilton et al. (1995). This was done both with our finite difference code, and with David Clarke's version of ZEUS3D, for comparison purposes. We checked the nonlinear transition mechanism was well reproduced, with the corresponding Reynolds number and aspect ratio, and that the two codes gave completely consistent results. Then, the shearing sheet boundary conditions were tested using these two finite difference codes and the Fourier code. We have verified that mean turbulent quantities (e.g., mean energy, mean transport, velocity maxima and minima) and critical Reynolds number were statistically the same using the different codes, for different rotation numbers, either cyclonic or anticyclonic. This consistency holds over the $10^5 - 10^6$ time steps of our simulations.

3.2. Initial conditions and numerical strategy

The experimental results recalled in Sect. 2.4 suggest that a steep dependence of the transition Reynolds number with the rotation number may be the cause of the difficulty to find such

a transition in the previously published shearing sheet numerical simulations. Accordingly, one of the major aims of this investigation is to quantify the effect of the simulation resolution on the determination of the transition Reynolds number as a function of R_Ω.

Now, one of the characteristic features of the subcritical transition to turbulence is an observed spread in transition Reynolds numbers, depending on the choice of initial conditions, and a correlative large spread in turbulence life-times. This has been documented both experimentally (Darbyshire & Mullin 1995) and numerically (Faisst & Eckhardt 2004) in pipe flows, and guides to some extent our choice of initial conditions and our numerical procedure. Indeed, turbulent life-times typically vary from fast decay (survival for less than one hundred dynamical times) to long or indefinite survival (several thousands of dynamical times, with a clear divergence at finite Reynolds number) over several orders of magnitude of variation of the initial condition amplitude, but for less than 50% of variations of Reynolds number (see Faisst & Eckhardt 2004, Figs. 2 and 7).

It is reasonable to assume that this qualitative behavior is generic. Consequently, we have chosen once and for all, fixed, high amplitude initial conditions, to make our numerical runs more directly comparable to one another upon variations of Reynolds numbers. Furthermore, we consider that turbulence is long-lived if it is not observed to decay for 100 or 200 shear times (depending on the runs). This choice is a compromise between computational time constraints, and accuracy in the determination of the transition Reynolds number of indefinitely self-sustained turbulence. In practice, simulations are performed in a cubic box (the impact of this choice is discussed in the next section, to some extent). The flow is adimensionalized with the only dimensional quantities introduced in the problem: S and d, where d is the simulation box size (or equivalently, by choosing $|S| = 1$ and $d = 1$). The initial conditions used for all our simulation are a random 3D excitation of the 10 largest Fourier modes, with rms fluctuations in velocity of order unity in our chosen units. Other shapes of initial conditions were tested such as white noise (all scales excited randomly) or introducing large scale vortices in various directions with a small superimposed noise. This produces no significant difference once the flow is relaxed ($t \gtrsim 20\,t_s$).

The numerical strategy adopted is then rather straightforward: choosing a code, a resolution, a boundary condition (for the finite difference code) and a Reynolds number, at fixed initial conditions, the flow evolution is computed starting from the marginal stability limit in rotation number R_Ω and evolving the rotation number by (small) fixed steps every 100 or 200 shear times. According to the preceding discussion, this allows us to reduce at maximum the number of runs and the run time needed to observe systematic trends in the numerical results.

In this section, only shearing sheet boundary conditions are used. We have also checked that the time required to dissipate the turbulent energy of the flow assuming energy injection is stopped (deduced from the ϵ term in Eq. (6)) is smaller than $100t_s$; this constraint is always satisfied by a large margin in all our runs, implying that the deviations from laminar motion that we observe are self-sustained (i.e., we do not

---

[3] We thank Achim Wirth for pointing out this reference to us.
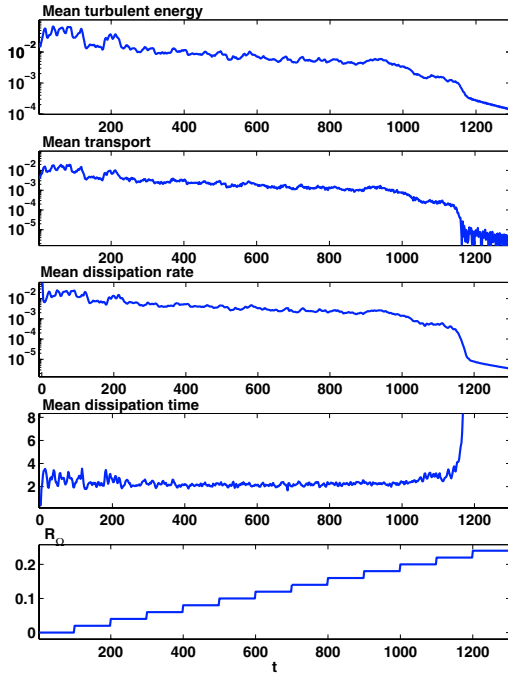
Fig. 3. Example of the time evolution of a 64^3 (Re = 12 000) cyclonic flow run as computed by our Fourier code. The turbulent energy, transport and dissipation rate are the quantities involved in Eq. (6). The dissipation time follows from the turbulent energy and the dissipation rate. The bottom panel displays the evolution of the rotation number that is imposed in the course of the simulation.

observe them because their dissipation time exceeds the run time). Actually, once turbulence is lost in our simulations, the energy in the velocity fluctuations always decreases rather fast, as can be checked in Fig. 3 for cyclonic flows. The same property is found for anticyclonic flows, see Sect. 3.4.

We conclude this section on our choice of the Mach number (Ma = dS/c_s) for our simulations with the compressible Zeus-like code. The type of motions we are considering in these simulations reach at most a small fraction of the boundaries relative velocity (normalized to unity in this work). We found that a sound speed also normalized to unity was a good compromise between limiting the effects of compressibility (which eventually makes the turbulence compressible and largely different in character when the Mach number is too large), and the impact of the sound speed on the CFL condition. Also, this value mimics the real role of compressibility in a vertically stratified accretion disk. Consequently, Ma = 1 is imposed in all our compressible simulations.

3.3. Numerical results: cyclonic flows

On the cyclonic side, simulations are performed while maintaining the rotation number R_Ω constant during 100 shear times; then the rotation number is increased by steps of 0.02, starting from the marginal cyclonic point $R_\Omega = 0$. An example global output of such a simulation is plotted in Fig. 3
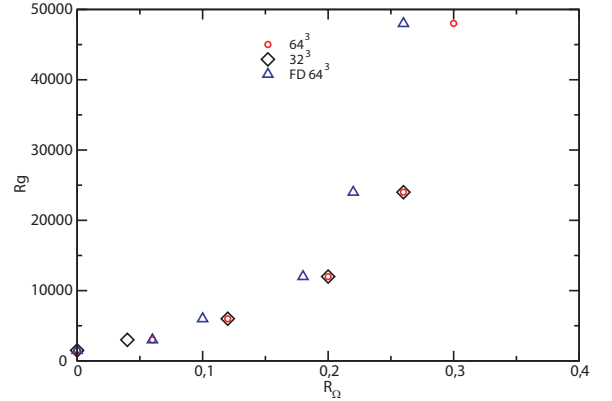
Fig. 4. Transition Reynolds number Rg as a function of the rotation number R_Ω, with different resolutions and codes for shearing-sheet boundary conditions (cyclonic rotation). All points were obtained using our Fourier code except those labelled FD (finite difference) which use our ZEUS-like code.

for Re = 12 000. The relaminarization point is easily found since the transition between the turbulent to laminar state is quite abrupt (at $t = 1150$ in Fig. 3). We define the last turbulent point as the last rotation rate for which turbulence is sustained for $100\,t_s$. For our example simulation, we find that the last turbulent point at Re = 12 000 and 64^3 resolution with our Fourier code is $R_\Omega = 0.2$.

Using this kind of simulation, we plot the last turbulent points in the (Re, R_Ω) space, for different resolutions and/or codes in Fig. 4. Turbulence is found on the cyclonic side at least up to $R_\Omega = 0.3$, i.e. significantly away from the marginal stability point.

Note that turbulence is maintained with certainty (with our adopted criteria) at any given point, but, due to the sampling made in the explored Reynolds number, turbulence may also be maintained at a somewhat lower Reynolds number (i.e. just below the last turbulent point in Fig. 3). This can be true down to the previously tested Reynolds number, for which turbulence is not maintained at the considered rotation rate. In conclusion, the real transition Reynolds Rg curve in the (R_Ω, Re) plane should be found somewhat below (but not far from) the last turbulent point curve determined here. This remark is more important for anticyclonic flows, for which precise quantitative results are needed.

Except for a systematic shift between the results obtained with the Fourier code and the ZEUS-like one, the results seem to be independent of the resolution. The numerically minded reader may ask how one can reach such high Reynolds numbers with such relatively small resolutions. This point is addressed in Sect. 4.4.

An important issue is to quantify transport in subcritical turbulent flows. The phenomenological arguments of Longaretti (2002) suggest that $\langle v_x v_y \rangle \propto 1/Rg$ in subcritical flows, and that the turbulent transport in a given flow with specified (Re, R_Ω)

32   G. Lesur and P.-Y. Longaretti: Subcritical turbulence in rotating shear flows
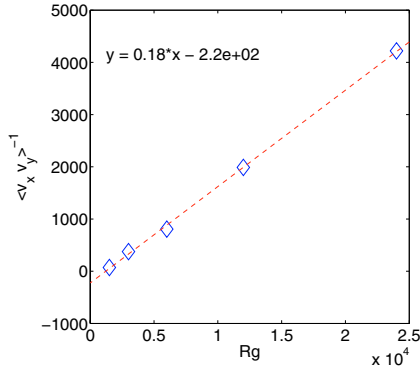
Fig. 5. Mean transport as a function of the transition Reynolds number for cyclonic rotation (normalized by $S^2 d^2$).

numbers depends only on R_Ω through Rg (see Sect. 4.1)[4]. Consequently, we have used all our simulations at a given R_Ω to obtain the least noisy evaluation of $\langle v_x v_y \rangle$. Then, with the help of Fig. 3, one finds a transition Reynolds number Rg for any given R_Ω, which allows us to plot the mean turbulent transport $\langle v_x v_y \rangle$ as a function of the transition Reynolds number in Fig. 5. This was done only from the data of our Fourier code for self-consistency, but using both the 32^3 and 64^3 resolution runs, as they produced the same results, and as the use of a larger data set improves the statistics. The resulting relation reads

$$\langle v_x v_y \rangle \simeq \frac{5.5}{Rg - 1250}(S\,d)^2. \tag{19}$$

The presence of an additive constant in the denominator of this expression is a clear indication of the influence of the linear instability close to the marginal stability limit; indeed, transport in the supercritical region is significantly enhanced with respect to the subcritical region (see, e.g., Fig. 16 in Dubrulle et al. 2005a, and explanations therein). For large critical Reynolds number (i.e., far enough from the marginal stability boundary, e.g., $Rg \gtrsim 15\,000$), $\langle v_x v_y \rangle \simeq 5.5/Rg$ is a good approximation.

3.4. Numerical results: anticyclonic flows

The strategy adopted in simulations of anticyclonic flows is similar to the cyclonic side. Starting at $R_\Omega = -1.0$, the rotation number is decreased in steps of 0.004 and each step lasts 200 shear times to allow for flow relaxation. A typical run is shown in Fig. 6, computed with our 3D Fourier Code at Re = 12 000. One should note that the flow fluctuations have higher amplitudes on the anticyclonic side than on the cyclonic side; this is why we have reduced the rotation number steps and increased the relaxation time in anticyclonic runs. Consistently, The last turbulent point is defined here as the last rotation rate for which turbulence is sustained for $200t_s$. On the

---

[4] The same result follows if one assumes that in the fully turbulent state, the torque $\propto \mathrm{Re}^2$, as predicted in Kolmogorov turbulence, and observed in experiments (see, e.g., Dubrulle et al. 2005a). The argument of Sect. 4.1 allows us to recover this result from more generic physical principles.
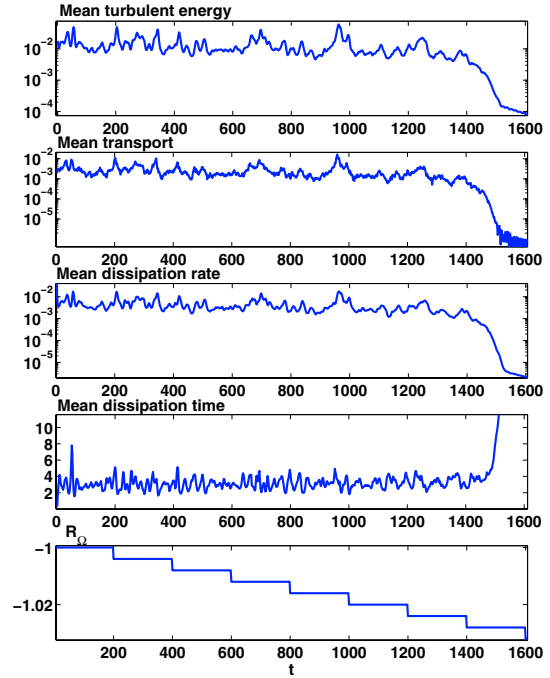

Fig. 6. Time evolution of a 64^3 Re = 12 000 anticyclonic flow as computed by our Fourier code. Panel description is identical to Fig. 3.

example Fig. 6, we find the last turbulent point for Re = 12 000 at $R_\Omega = -1.024$.

As for cyclonic rotation, the last turbulent points for anticyclonic rotation are plotted in Fig. 7 and the mean transport in Fig. 8. Error bars are added in Fig. 7 to help assessing the significance of the various fits performed, as they will be used later on. On the lower bound of these bars, turbulence is not maintained with certainty whereas the contrary is true for *at least* 200 shear times at the upper bound. Therefore, the actual transition Reynolds number is bracketed by the error bar.

Recalling that $R_\Omega = -2/q$ with $\Omega(r) \propto r^{-q}$ and that $R_\Omega = -1$ corresponds to a constant specific angular momentum distribution in cylindrical flows, the largest rotation number reached here ($R_\Omega = -1.032$) corresponds to $q = 1.94$; this is quite consistent with the results shown in Fig. 1 of Hawley et al. (1999), except for the crucial fact that the resolution and Reynolds number dependence are now quantified. The reason why such high Reynolds numbers are accessible with our relatively low resolutions is discussed in Sect. 4.4. For the time being, let us comment a bit further on the information encoded in Fig. 7, which shows that Reynolds number and resolution are different, albeit related control parameters. We will focus on the Fourier code data for definiteness. Consider the 32^3 data, for example. For $|R_\Omega| < 1.016$, the transition Reynolds number agrees with the one found at higher resolution. However, increasing the Reynolds number above ~6000 produces a loss of turbulence at the same rotation number independently of the Reynolds number, whereas this is not true at higher resolutions. This implies that the physics is not faithfully represented at this resolution for Re > 6000 and $R_\Omega > 1.016$.
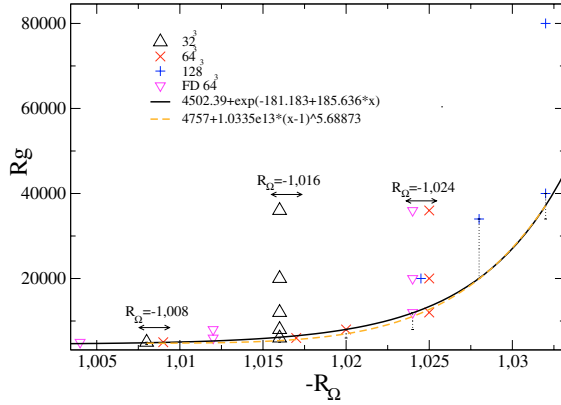
Fig. 7. Transition Reynolds number Rg as a function of the Rotation number R_Ω, and related analytical fits, with different resolutions and codes for shearing-sheet boundary conditions (anticyclonic side). All plots were computed using our Fourier code except FD (finite difference) which uses our ZEUS-like code. Note that the x-axis is inverted with respect to Fig. 2. Symbols along the fitted lines correspond to resolved simulations; vertically aligned symbols indicate the limiting rotation number that can be reached at a given resolution and mostly correspond to unresolved simulations. For the sake of clarity, symbols which sit on top of each other have been slightly displaced along the R_Ω axis; this is indicated by the arrows and the related values of R_Ω.

This is the most important point to note here: two different regimes of transition from turbulent to laminar are displayed in this figure. The first (corresponding to the various fitting curves) is the correct, resolution independent and Reynolds dependent transition. The second (apparent as the various vertically aligned points at a given resolution) is an incorrect, Reynolds independent and resolution limited transition. Note that the points belonging to both this vertical line and the laminar-turbulent line are still resolved, though, as shown in Sect. 4.4.2. The meaning of the behavior displayed in Fig. 7 is further discussed in Sect. 4.1, and its implications in Sects. 4.2 and 4.4.

Comparing Figs. 4 and 7, we remark that the dependence of the transition Reynolds number Rg on the "distance" to marginal stability in rotation number $|R_\Omega - R_\Omega^\pm|$ is considerably stiffer on the anticyclonic side than on the cyclonic one. This has important implications that will be discussed in the next section. Conversely, the turbulent momentum transport is very similar to the one found for the cyclonic side[5], as shown in Fig. 8

$$\langle v_x v_y \rangle \simeq \frac{5.5}{Rg - 3000}(S d)^2. \tag{20}$$

The constant in the denominator differs from the one found on the cyclonic side. This reflects the difference of transition Reynolds number at the two marginal stability limits. For large enough Reynolds number, one find $\langle v_x v_y \rangle \simeq 5.5/Rg$, which
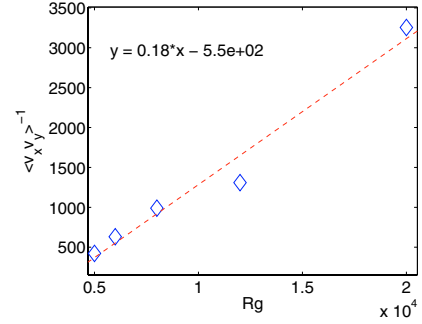
Fig. 8. Mean transport as a function of critical reynolds number on the anticyclonic side (normalized by $S^2 d^2$).

corresponds to the asymptotic relation found on the cyclonic side (see Sect. 4.1 for a discussion of the possible origin of this behavior). This indicates that this relation is very robust for subcritical flows, far enough from the supercritical transition limit.

4. Discussion

Our results are at variance with both the point of view advocated by Balbus et al. (1996) and Hawley et al. (1999) (absence of subcritical turbulence), and Richard & Zahn (1999) and Hersant et al. (2005) (efficient transport due to subcritical turbulence). This is further investigated in this section. We shall first present some phenomenological background material which helps to understand the physical origin and meaning of the results presented in the previous section. Then, we shall respectively discuss the implications of our results for Keplerian flows (Sect. 4.2), the stabilizing role of the Coriolis force in subcritical flows (Sect. 4.3), and the relation between Reynolds number and resolution (Sect. 4.4); these last two items have been highly controversial in the past decade. Section 4.4 also discusses the relation of these results with the scale-invariance argument of Balbus (2004). Finally the influence of the nature of the adopted boundary conditions and aspect ratio on our results is the object of Sect. 4.5, as well as their relation to fluid dynamics experiments. Note also that the discussion of the boundary conditions helps quantifying possible biases introduced by the sheering sheet boundary conditions with respect to actual disk physics. The reader interested only in the astrophysical implications of our results may focus in Sect. 4.2.

4.1. Some aspects of subcritical turbulence phenomenology

The phenomenology of subcritical turbulence has been discussed in Longaretti (2002) and Longaretti & Dauchot (2005). Some directly relevant aspects for our present purpose are presented here (and clarified where needed).

Turbulent transport is often quantified in terms of a turbulent viscosity. As this description has been criticized in the past, a brief discussion of its use here might be useful. First, note that, in scale-free systems such as the ones studied here (the

---

[5] Figure 8 is noisier than its cyclonic counterpart. This is a consequence of the larger turbulent fluctuations observed in anticyclonic flows. Longer integrations time-scale would have been required to improve the statistics.

only scale present being the simulation box size), one can always assume that

$$\langle v_x v_y \rangle = \nu_{\mathrm{t}} S, \tag{21}$$

as this only amounts to defining a turbulent viscosity ν_{t} such that this relation is satisfied. In any case, as the source of turbulence is the shear, the Reynolds stress $\langle v_x v_y \rangle$ *must* be some function of the shear S, which cancels when the shear cancels.

Now, ν_{t} has the dimension of a length times a velocity, so that one must therefore have, in our simulations,

$$\nu_{\mathrm{t}} = \alpha S d^2, \tag{22}$$

as $S d$ and d are the only dimensional quantities with the right dimensionality introduced in the problem.

α is a Shakura-Sunyaev-like parameter. It is a dimensionless quantity, and can therefore only depend on the dimensionless quantities[6] characterizing the problem at hand, namely the Reynolds number Re and the rotation number R_Ω (i.e., the shear dependence of α can only appear through the ratios of the shear time scale to the viscous and the rotation time scales):

$$\alpha \equiv \alpha(\mathrm{Re}, R_\Omega). \tag{23}$$

The results of Sect. 3 suggest that, quite remarkably, α depends only on R_Ω through the transition Reynolds Rg, and not (or little) on Re, in subcritical flows. The origin of this behavior can be understood in the following way (Longaretti 2002).

A sheared flow is out of global thermodynamical equilibrium, and tries to restore this equilibrium by transporting momentum across the shear. A subcritical flow has only two means at its disposal to achieve this purpose: laminar and turbulent transport. It will tend to choose the most efficient one under any given set of conditions[7], i.e. at given Re and R_Ω. The subcritical turbulent transport will exceed the laminar one when $\nu_{\mathrm{t}} \gtrsim \nu$. Right at the laminar-turbulent threshold, Re $\sim Rg$ and $\nu_{\mathrm{t}} \sim \nu$. This implies that
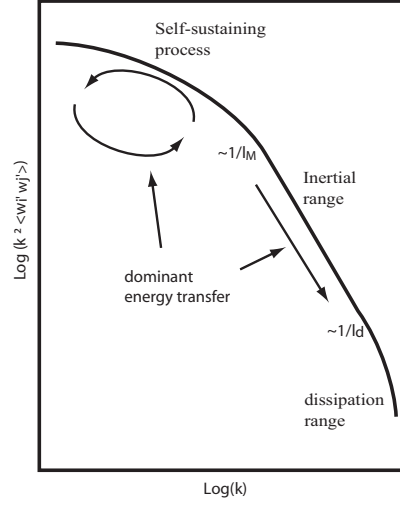
$$\alpha \sim \frac{\nu}{S d^2} \sim \frac{1}{Rg}. \tag{24}$$

Now, what does happen at Reynolds numbers Re *larger* than the transition Reynolds number Rg? To answer this question, it is useful to have in mind some idealized, qualitative picture of the situation in wave-number space. Such a picture is proposed in Fig. 9, and constitutes a reasonable working hypothesis. It is reasonably well-supported by our current knowledge of the plane Couette flow turbulent self-sustaining process and of inertial spectra, as well as by the spectral analysis of some of our simulations presented and discussed in Sect. 4.4.2.

In this picture, the large scales are occupied by the self-sustaining mechanism. All scales in this domain are expected to be coherent in phase, and interactions between large and small

Fig. 9. Proposed sketch of the idealized energy spectrum in a turbulent shear flow. Arrows indicate the energy flow through mode coupling. The length-scales l_M and l_{d} correspond to the top of the inertial range (assumed identical to the bottom of the self-sustaining range for simplicity) and the top of the dissipation range. Scales are assumed to be normalized to the box simulation size d, and anisotropy is ignored in this sketch (see text for details).

scales occur both ways[8]. The intermediate range is the inertial range of turbulence; scales have no phase coherence, energy cascades to smaller scales at a constant rate, provided by the self-sustaining mechanism (as part of the mode coupling taking place in the self-sustaining mechanism range of scales occurs with the inertial range). The smallest range represents the viscous dissipation scales. The existence of the self-sustaining process scales, their properties, and their influence on the inertial range (energy input and anisotropy) is the distinctive feature of shear turbulence with respect to the more commonly known and studied forced isotropic turbulence.

In such a picture, increasing the Reynolds number almost exclusively results in an increase of the inertial range, which is essentially vanishing at the transition Reynolds number. This should have little effect on the turbulent transport (whereas, on the contrary, the laminar transport becomes smaller and smaller when increasing the Reynolds number).

Indeed, we have first checked that this is case in nonrotating Couette plane flows, where the self-sustaining mechanism is identified (Hamilton et al. 1995): the transport is almost completely determined dominated by the mechanism rolls and streaks. Furthermore, in our simulations, we have computed the contribution of each length scale to the total transport $\langle v_x v_y \rangle$. First one should note that in Fourier space (in 1D for simplicity):

$$\langle v_x v_y \rangle = \sum_{n=0}^{N-1} \tilde{v}_x(k_n) \tilde{v}_y^*(k_n). \tag{25}$$

---

[6] Actually, in principle, α depends also on the aspect ratio of the simulation, and on the nature of the boundary conditions. As these are not varied in the results discussed on the basis of the phenomenology described here, this dependency is ignored for simplicity.

[7] Note that this does not imply that the momentum transport is absolutely maximized.

[8] This is the case in particular for the non-rotating plane Couette self-sustaining mechanism (Waleffe 1997).
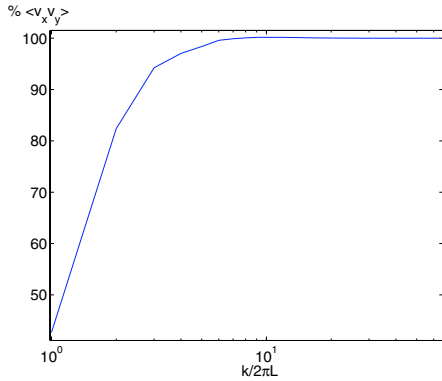
Fig. 10. Example of the cumulative sum contribution of each scale length to the mean transport, starting from $k_x = 0$ in the x direction: 99% of the transport comes from $k_x < 10$ scales. From a 128^3 simulation, Re = 20 000, $R_\Omega = -1.020$.

Therefore, the contribution to mean transport of the wavelength k_n is found to be $2\Re\left(\tilde{v}_x(k_n)\tilde{v}_y^*(k_n)\right)$, since k_n and k_{N-n} represents the same physical wavenumber. This simple result can be used in 3D by averaging the transport over 2 directions (in physical space) and by computing the Fourier transform in the remaining direction; this procedure is sufficient for our purpose here. The resulting cumulative Fourier sum, starting from $n = 0$ is illustrated on an example in Fig. 10 to quantify which scales dominate the transport. In this example, the resulting spectral analysis is plotted in the x direction for a 128^3 anticyclonic flow with $R_\Omega = -1.024$ and Re = 20 000, showing that more than 99% of the transport comes from scales larger than 1/10 of the box size; this range corresponds to the length-scales of the self-sustaining process (see Sect. 4.4.2). Similar results are found for spectral analyzes in the y and z directions, consistently with the picture discussed here. This is expected anyway if the inertial spectrum is Kolmogorovian, as confirmed from the spectral analysis of Sect. 4.4.2[9].

There are two loose ends in this discussion. First, hysteresis is usually experimentally observed in subcritical transitions to turbulence: the measured transition Reynolds number is higher when moving "up" from the laminar to turbulent states than when moving "down" from the turbulent to laminar ones. This suggests that the laminar-turbulent boundary is separated by some sort of barrier in the appropriate phase-space (defined, e.g., by the amplitudes and phases of the Fourier modes). This (along with the fact that the arguments developed here apply only in order of magnitude) may well explain the existence of the constant of order 5 that one finds in Eqs. (19) and (20) with respect to Eq. (24). Secondly, the arguments presented here ignore the existence of marginal stability thresholds. This, as pointed out in Sects. 3.3 and 3.4, may explain the presence of the constant at the denominator of these relations, as the equivalent global subcritical transition Reynolds number that one

can define in the supercritical regime is orders of magnitude smaller than in the subcritical regime.

To conclude, let us point out the relation of this picture with the numerical results presented in Fig. 7. The fact that higher resolutions are required to faithfully represent the physics at higher rotation numbers indicates that the ratio d/l_M increases with rotation number. Indeed, if the resolution is too low, so that the relative scale l_M/d is not resolved, the energy transfer loop represented in Fig. 9 cannot take place, and turbulence is not self-sustained. Furthermore, at the transition Reynolds number, the inertial spectrum is nearly inexistent, as pointed out above, and $l_M \sim l_d$. Consequently, the most critical scale ratio in this problem is expected not to be the Kolmogorov one, but the self-sustaining mechanism one (d/l_M).

4.2. Implications for Keplerian flows

Actual disks are vertically stratified, whereas stratification is ignored in our experiments. Stratification provides us with a local macroscopic scale (the disk scale height H). With appropriate provisos relating to the possible stabilizing or destabilizing role of stratification[10], one can tentatively identify this scale height with our simulation box size: $H = d$. This assumption is made throughout this section. In the same way, the Shakura-Sunyaev α_{SS} parameter is defined such that $\nu_t = \alpha_{SS} c_s H \simeq \alpha_{SS} \Omega H^2$. Equation (22) then implies that $\alpha_{SS} = 2\alpha/|R_\Omega| \simeq \alpha$ (the last equality holds within a factor of order unity for the rotation number range of interest in this work).

Using the numerical results shown in Figs. 7 and 8, one can deduce a few properties of Keplerian flow subcritical shear turbulence, based on various conservative extrapolations of our numerical data. First, the transition Reynolds number Rg dependence on the rotation number R_Ω is well-fitted by a power or an exponential law. Using these laws, one can get a first set of estimates of the transition Reynolds number for Keplerian-like flows ($R_\Omega = -4/3$): $Rg = 1.1 \times 10^{10}$ and $Rg = 1.3 \times 10^{26}$, respectively. The last estimate leads to the absence of subcritical turbulence in accretion disks whereas the first one allows for its existence[11]. Secondly, let us note that, for both cyclonicity, the Coriolis force induces a steeper and steeper increase of the transition Reynolds number when moving away from the marginal stability boundary. This suggests that one can find a lower bound for Rg by linearly extrapolating the power law fit beyond the last known point ($R_\Omega = -1.032$). One find this

---

[9] The true nature of the inertial spectrum might be affected by the anisotropy generated by the the shear and the Coriolis force, but these anisotropies must become negligible at small scale, due to the shorter and shorter eddy turnover time.

[10] If stratification is destabilizing, the momentum transport induced by the resulting convective motions is in the wrong direction, as recalled in the introduction, and must be counterbalanced by another process; ignoring stratification in this case therefore makes life easier for this other process (here, subcritical turbulence). If stratification is stabilizing, this also most likely results in an increased difficulty in finding the transition to turbulence, and a related increase in the transition Reynolds number. These arguments suggest that ignoring the dynamical stratification altogether maximizes the overall outwards transport in our problem.

[11] We assume that accretion disk Reynolds numbers lie between 10^{10} and 10^{15} for definiteness. The Reynolds number definition used in this evaluation is Re = SH^2/ν where H is the local disk scale height, consistently with the $H = d$ identification made earlier.

Table 1. Extrapolated transition Reynolds numbers, values of α, and required simulations resolution, for Keplerian flows, under various assumptions (see text for details).

	exponential	power-law	cyclonic	linear
Rg	1.3×10^{26}	1.1×10^{8}	2×10^{7}	1.8×10^{6}
α	n/a	5×10^{-10}	2.6×10^{-7}	3.1×10^{-6}
$(d/\delta)^{3}$	n/a	7000^{3}	3000^{3}	900^{3}

way $Rg^{\min} = 1.8 \times 10^{6}$. As a final hypothesis, one may envision that the $Rg(R_{\Omega})$ relation would be more or less symmetric with respect to $R_{\Omega} = 0$ if there were no supercritical domain. This would explain why the actual relation of Fig. 7 is so steep: in this picture, the system tries to reach back as fast as possible the high values of transition Reynolds number expected from this hypothetical symmetry, after which the Reynolds dependence with rotation number would be much less steep. Under this assumption the expected transition Reynolds number for Keplerian flows would be $Rg = 2. \times 10^{7}$ (a power-law fit of the cyclonic data has been used in this extrapolation).

This information is summarized in Table 1, along with the corresponding values of α, obtained from the asymptotic relation $\alpha = \langle v_x v_y \rangle = 5.5/Rg$ found for cyclonic and anticyclonic flows in the previous section. The last line shows the resolution required to successfully simulate Keplerian flow turbulence, for the various Reynolds numbers (see Sect. 4.4.1). One sees that even the most optimistic α bound ($\alpha_{\max} = 3.1 \times 10^{-6}$), obtained with the linear extrapolation, is substantially smaller than the values required in astrophysical accretion disks (as summarized, e.g., in Papaloizou & Lin 1995). Note finally that, even without any extrapolation, our results exclude subcritical turbulent transport at the $\alpha \simeq 3 \times 10^{-4}$ level.

4.3. Role of the Coriolis force in uniform shear flows

Two different but related issues have been raised in the literature concerning the role of the Coriolis force in subcritical systems.

First, for linearly stable flows, Balbus et al. (1996) point out that the Coriolis force plays a conflicting role in Eqs. (4) and (5). More precisely, they make the following point: as $S \langle v_x v_y \rangle > 0$ for turbulence to exist (see Sect. 2.2), the terms in which the shear S has been factored out in these equations have opposite signs for linearly stable flows, while they have the same sign for linearly unstable flows (note that this is true independently of the flow cyclonicity). They conclude from this that a stabilizing rotation prevents turbulence to show up in subcritical shear flows, except possibly in the vicinity of marginal stability. Somewhat relatedly, the recent Reynolds stress-closure model of Ogilvie (2003) and Garaud & Ogilvie (2005) predicts relaminarization for large enough deviations from the marginal stability limit. In particular, for the authors' standard choice of parameters, it predicts relaminarization for $R_{\Omega} \sim 0.2$ for cyclonic rotation. However, as can be seen in Fig. 4, both the Balbus et al. (1996) argument and the Garaud & Ogilvie (2005) result conflict with our simulations: subcritical turbulence is

maintained away from marginal stability on the cyclonic side, at least up to $R_{\Omega} \simeq 0.3$. Note that we could have pushed the search for transition to turbulence beyond what is shown on this graph, especially by using higher resolutions, but did not do it due to computer resources limitations. As discussed in the next subsection, the absence of turbulence in the Keplerian flow simulations of Balbus et al. (1996) and Hawley et al. (1999) is a problem of resolution.

The second issue relates to the asymmetry between cyclonic and anticyclonic rotation. The stress-closure model just mentioned depends on the rotation number only through the combination $R_{\Omega}(R_{\Omega} + 1)$ which implies a symmetry with respect to $R_{\Omega} = -1/2$. This symmetry is clearly violated by our numerical results (compare Figs. 4 and 7), a point which requires some comments.

First, note that the linearized Navier-Stokes Eq. (1) exhibits this symmetry for perturbations with vanishing pressure variation ($\delta\pi = 0$). In this case, the linearized equation can be written:

$$\frac{\partial \boldsymbol{w}}{\partial t} = S \cdot y \frac{\partial \boldsymbol{w}}{\partial x} + S \cdot \left((R_{\Omega} + 1)w_y \boldsymbol{e}_x - R_{\Omega} w_x \boldsymbol{e}_y \right) + \nu \Delta \boldsymbol{w}. \quad (26)$$

The cyclonic-anticyclonic symmetry appears when exchanging the x and y directions. Indeed, upon the following change of variables:

$$R'_{\Omega} = -R_{\Omega} - 1,$$
$$w'_x = w_y, \qquad \boldsymbol{e}'_x = \boldsymbol{e}_y,$$
$$w'_y = w_x, \qquad \boldsymbol{e}'_y = \boldsymbol{e}_x,$$
$$w'_z = w_z, \qquad \boldsymbol{e}'_z = \boldsymbol{e}_z,$$

so that

$$\boldsymbol{w}' = w'_x \boldsymbol{e}'_x + w'_y \boldsymbol{e}'_y + w'_z \boldsymbol{e}'_z$$
$$= \boldsymbol{w},$$

the form of Eq. (26) should be invariant, which is indeed the case:

$$\frac{\partial \boldsymbol{w}'}{\partial t} = S \cdot y \frac{\partial \boldsymbol{w}'}{\partial x} + S \cdot \left((R'_{\Omega} + 1)w'_y \boldsymbol{e}'_x - R'_{\Omega} w'_x \boldsymbol{e}_y \right) + \nu \Delta \boldsymbol{w}'. \quad (27)$$

This symmetry can also be extended to compressible motions by adding $\delta\pi'(x, y, z) = \delta\pi(y, x, z)$ to the list of change of variables.

Because the perturbations defining the linear stability limit also exhibit this symmetry (Appendix A), it has often been assumed in closure-stress models in the past. However, this is not a symmetry of the full Navier-Stokes equation (Speziale & Mhuiris 1989; Speziale 1991; Salhi & Cambon 1997), nor of the $\boldsymbol{\nabla} \cdot \boldsymbol{w} = 0$ equation). This is also apparent in a direct inspection of the structure of simulated turbulent flows. The $R_{\Omega} = 0$, wall-bounded turbulent flows contain large *streamwise* rolls living for about a hundred shear times (Hamilton et al. 1995). We have also found rolls more or less aligned in the streamwise direction in our $R_{\Omega} = 0$ shearing sheet simulations, although we did not try to precisely quantify their survival time. Furthermore, at the anticyclonic marginal stability limit ($R_{\Omega} = -1$), we did observe sheared *shearwise* rolls (i.e. rolls in y direction) in our simulations, as one might expect

from the symmetry of the linearized Navier-Stokes equation. The anticyclonic roll survival time is observed to be rather short compared to their cyclonic counterpart, as they are tilted by the shear and loose their coherence in a few shear times at most. This roll lifetime is the main difference we found between the cyclonic and anticyclonic side. This is related to the fact that a streamwise roll does not reduce the shear on the anticyclonic subcritical domain (in opposition to the cyclonic one).

In any case, we have found turbulence away from the marginal stability limit in cyclonic flows, and the symmetry with respect to $R_\Omega = -1/2$ is violated both in our simulations, and in supercritically rotating shear flow turbulence (see, e.g., Salhi & Cambon 1997 and references therein). This make the predictions of the stress-closure model of Ogilvie (2003) and Garaud & Ogilvie (2005) unreliable in both subcritical and supercritical flows.

4.4. Resolution, effective Reynolds number and scale invariance

The results of Sects. 3.3 and 3.4 involve fairly high Reynolds numbers, and one might ask if our simulations are resolved enough in these regimes. This question has a priori two different aspects, as one can guess from Fig. 9: resolving the self-sustaining process smallest relative scale d/l_M, and resolving the relative dissipation scale d/l_d.

For the problem considered in this paper, resolving the first scale is a *sine qua non* condition: if it is not satisfied, turbulence does not show up, independently of the simulation Reynolds number, because the required scale coupling shown in Fig. 9 for the self-sustaining process to exist cannot take place. This shows up in Fig. 7 as the vertical transition limit from turbulent to laminar that we obtained for any given resolution, for large enough Reynolds numbers.

Resolving the dissipation scale is important to ascertain that direct numerical simulations such as the ones performed here are not biased by (the presence or absence of) numerical dissipation, and this issue is often raised in the fluid mechanics literature. For the time being, we note that, at the transition Reynolds number, the inertial domain should be non-existent or extremely reduced, so that $l_M \simeq l_d$ and both resolution requirements should be directly related (this point, used in Sect. 4.4.1 is justified in Sect. 4.4.2). We can therefore consider that the "effective Reynolds number" Re_eff of our simulations is the largest transition Reynolds number Rg correctly determined at a given resolution[12], as discussed in Sect. 3.4.

Note that this effective Reynolds number is problem-dependent: the self-sustaining process qualitative and quantitative characteristics both depend on the considered problem; furthermore, in simulations of isotropic turbulence, the self-sustaining process is absent, and replaced by a forced amplitude of the largest Fourier modes, so that the effective Reynolds number in this case is the one related to the dissipation scale.

---

[12] With all the provisos discussed in Sect. 3.2 about the role of the choice of the initial conditions and turbulence minimal survival lifetime.

Let us now examine the two requirements mentioned above in more detail.

4.4.1. Resolving the self-sustaining process

First, we would like to qualitatively comment on the difference of resolution requirements between cyclonic and anticyclonic flows.

As discussed in Sect. 4.5, the nature of the shearwise boundary condition has apparently only a small influence on the results; this is exemplified by the similar transition Reynolds numbers found in our simulations and in experiments on rotating shear flows (see Fig. 14). This suggests that at least some of the characteristics of the self-sustaining process of non-rotating plane Couette flows are relevant here. At the cyclonic marginal stability limit, this self-sustaining process has a time-scale $t_\mathrm{SSP} \sim 100 S^{-1}$ (Hamilton et al. 1995; Waleffe 1997). The requirement that, at the transition Reynolds number, the viscous time scale at scale l_M exceeds t_SSP reads $l_M^2/\nu \gtrsim 100 S^{-1}$, i.e., $l_M/d \lesssim (100/Rg)^{1/2} \sim 1/4$ for $Rg \sim 1500$ (Longaretti & Dauchot 2005). This probably explains why the resolution requirement is so low on the cyclonic side. Conversely, we have mentioned at the end of the previous subsection that rolls (which are an apparently ubiquitous ingredient in subcritical turbulence) do not survive more than a few shear times in anticyclonic flows. Therefore, the anticyclonic self-sustaining process time-scale cannot exceed a few shear times as well, whatever its nature. The same reasoning as the one exposed above leads to $l_M/d \lesssim$ a few $(1/Rg)^{1/2} \sim$ a few $\times 1/70$, an already much more demanding constraint. It is obviously related to the larger transition Reynolds number found at the anticyclonic marginal stability, compared to the cyclonic one.

As mentioned several times already, the self-sustaining process is identified and understood only at the cyclonic marginal stability limit in wall-bounded Couette flows. Consequently, it is difficult to explain why the resolution demand grows so much faster with rotation number "distance" to marginal stability for anticyclonic flows than for cyclonic ones. However, we speculate that this is connected to the fact the rotation time scale is only a fraction of S^{-1} for cyclonic flows, whereas it always exceeds S^{-1} for anticyclonic ones.

Next, let us try to quantify the resolution that would be needed to successfully simulate Keplerian flows. The phenomenology of subcritical turbulence developed by Longaretti (2002) predicts that $d/l_M \sim Rg^{1/2}$ and $\langle v_x v_y \rangle \propto 1/Rg$. This phenomenology implicitly assumes that the relevant time-scale of the self-sustaining process is $\sim S^{-1}$, so that it would need to be modified to be applied to cyclonic flows, but it should be adequate for anticyclonic ones, with appropriate modifications. In particular, we have already pointed out in Sect. 4.1 that the last relation needs to be amended into $\langle v_x v_y \rangle \propto 1/(Rg - R_c)$ with $R_c \simeq 3000$ on the anticyclonic side. This suggests that

$$\frac{\delta}{d} \simeq \frac{\gamma}{(Rg - R_c)^{1/2}} \qquad (28)$$

is the appropriately generalized scale relation (δ being the smallest scale accessible to the simulation, i.e., the resolution).

Table 2. Resolution, effective Reynolds number and γ factor for the Fourier code on the anticyclonic side.

$(d/\delta)^3$	$\mathrm{Re}_{\mathrm{eff}}$	γ
32^3	6000	1.71
64^3	12 000	1.48
128^3	38 000	1.46

Table 2 gives the values of γ and $\mathrm{Re}_{\mathrm{eff}}$ for the three different resolutions of our anticyclonic simulations.

Although the statistics is a little poor to draw firm conclusions, it appears that γ is nearly constant compared to the variations in both resolution and transition Reynolds number, and our simulations are therefore consistent with Eq. (28). The resolution needed to simulate Keplerian flows has been computed based on the estimate Eq. (28), with $\gamma = 1.5$ (the R_c correction has little influence on these estimates). The results are shown in Table 1. For comparison purposes, note that the largest turbulence simulation ever performed was 4000^3, but was not run for hundreds or thousands of dynamical times. Although the results gathered here are probably only indicative, as they are based on guess work, they strongly suggest that simulating subcritical turbulence in Keplerian flows is beyond present day computer capabilities, and support the idea that the subcritical Keplerian flows simulations performed to date were limited by numerical resolution, as suggested by Longaretti (2002).

4.4.2. Resolving the dissipation scale

In statistically steady turbulence, the dissipation scale can be defined from the balance between input and dissipation described by Eq. (8). The energy input is provided by $S\langle v_x v_y \rangle$. The Fourier analysis of this quantity is shown in Fig. 10, and is dominated by the large scales. Conversely, the Fourier content of ϵ, Eq. (7), is dominated by the small scales (large k), comparable to the dissipation scale, as illustrated below.

Resolving the dissipation scale is important with Fourier codes in order to prevent energy accumulation at the smallest scales, which may bias the results, or lead to code crash[13].

The general definition of the dissipation wavelength k_d follows from the evaluation of Eq. (7) in Fourier space:

$$\epsilon = 2\nu \int_0^{k_d} k^2 E(k) \mathrm{d}k \tag{29}$$

where it is assumed that $E(k)$ is cut-off at k_d, either abruptly, or through some modelling of the dissipation range (see e.g. Lesieur 1990).

In simulations of homogeneous and isotropic turbulence, the energy input is imposed from the outside: the amplitude of the largest Fourier mode is held fixed, and Fig. 9 reduces to the inertial and dissipation range. In this context, the inertial spectrum reduces to the Kolmogorov spectrum given by:

$$E_K(k) = C_K \epsilon^{2/3} k^{-5/3}, \tag{30}$$

where the Kolmogorov constant $C_K \simeq 1$. Cutting off this spectrum at wavelength k_d and injecting it in the definition Eq. (29) leads to the well-known expression of the Kolmogorov wave number, $k_K = (\epsilon/\nu^3)^{1/4}$. The related Kolmogorov scale (inverse of the wave number) is a largely used estimate of the dissipation scale.

In the fluid mechanics community one often requires that the Kolmogorov scale be resolved, even if the considered turbulence is not isotropic and homogeneous, as, e.g., in shear flow turbulence (see, e.g., Pumir 1996). However, in our simulations, the observed spectrum is substantially different from the Kolmogorov one, especially at the transition Reynolds number (see top panel of Fig. 12). Indeed, at the turbulent-laminar transition, one does not expect nor observe the presence of an inertial domain in the spectrum. One may therefore ask what relation the Kolmogorov scale bears to the dissipation scale of the problem.

Consider, e.g., the 32^3 and 64^3 energy spectra obtained at a Reynolds number Re = 6000 and a rotation number set to -1.016. These spectra are shown on the top panel of Fig. 12. The concordance of the spectra at both 32^3 and 64^3 resolutions indicates that the dissipation scale in the 32^3 simulation is resolved (this is consistent with the shape of the spectrum at the smallest 32^3 resolved scales, much steeper than Kolmogorov). It appears that the largest distance to marginal stability $|R_\Omega + 1|$ reliably accessible at a given resolution on the laminar-turbulent transition (as checked by higher resolution simulations) corresponds to the various vertical line of transition displayed in Fig. 7 for this resolution. In other words, the Re = 6000, $R_\Omega = -1.016$ point at 32^2, and the Re = 12 000, $R_\Omega = -1.024$ at 64^3, are resolved. This feature makes us confident that the transition point determined at 128^3 is the correct one, although we did not cross-check it at 256^3, due to the limitations in the available computational resources.

We have thus determined the largest transition Reynolds number where the dissipation scale is confidently resolved in these anticyclonic runs at the various resolutions we have used (32^3, 64^3 and 128^3). In other words, we know the effective dissipation scale of these simulations, as it must be comparable to the largest wave number available in the simulation[14]: $k_d \simeq 3^{1/2}\pi N/d$, where N is the resolution. Furthermore, we can compute the Kolmogorov wave number k_K for these runs, as $\nu = \mathrm{Re}/S\,d^2$, and as ϵ follows from Eq. (8) and the transport (e.g., with the help of the transport/transition-Reynolds-number correlation displayed in Fig. 8). The resulting ratio $R = k_d/k_K$ is given in Table 3.

Although the values of the ratio R quoted in Table 3 are of order unity, a systematic trend seems to appear, indicating that resolving the Kolmogorov wave number is possibly not the relevant concept at the transition Reynolds number, as it is not stringent enough; nevertheless, the required resolution derived from the Kolmogorov wave number is apparently semi-quantitatively correct, at least for the rotation numbers explored

---

[13] One may also include an hyper-viscosity term to prevent code crash, but this turned out not to be necessary.

[14] This expression corrects a misprint in Pumir (1996) for the diagonal of a cube in Fourier space; although this largest wave number is resolved only in discrete directions, this definition is adopted here for ease of comparison with this earlier work.

Table 3. Resolution, dissipation to Kolmogorov wave number ratio, and corresponding transition Reynolds number (see text for details).

N	$R = k_d/k_K$	Rg
32	1.23	6000
64	1.73	12 000
128	2.66	35 000
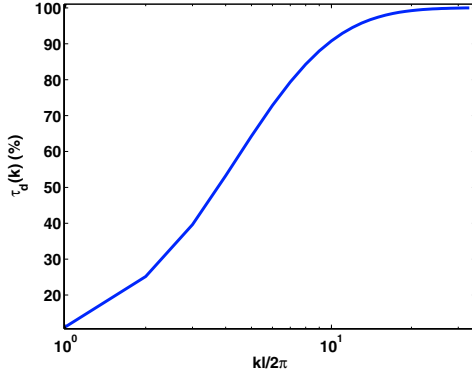
Fig. 11. Cumulative mean dissipation spectrum for a 64^3 simulation at Re = 6000 for $R_\Omega = -1.016$.

here. Of course when going to Reynolds numbers well in excess of Rg at a given R_Ω, the Kolmogorov wave number should always give the right estimate of the dissipation scale, as the inertial range becomes more and more prominent in the overall spectrum.

To conclude this aspect of the discussion, we note that both the non-Kolmogorovian shape of the spectrum at transition and the relatively small values of ϵ at the various transition Reynolds numbers used here, most probably combine in the end to explain why we can reach rather large Reynolds numbers at rather moderate resolutions.

In order to have a better grasp on which scales contribute most to the dissipation, we have computed a quantity, $\tau_d(k)$, defined by

$$\tau_d(k) = 2\nu \int_{-k}^{k} dk_x \int_{-k}^{k} dk_y \int_{-k}^{k} dk_z \left(k_x^2 + k_y^2 + k_z^2 \right) E(k_x, k_y, k_z). \quad (31)$$

Comparing with Eq. (29), it appears that $\tau_d(k)$ represents the fraction of dissipation due to scales $|k_x| < k$, $|k_y| < k$ and $|k_z| < k$. This quantity is plotted in Fig. 11 with the 64^3 simulation spectrum. It appears that more than 95% of the total dissipation is due to $k < 1/2k_{max}$ (i.e., the 32^3 resolution). Also, comparing Fig. 11 with the top panel of Fig. 12 indicates that most of the dissipation comes from the part of the spectrum which is steeper than the Kolmogorov spectrum, as one would expect.

It is also instructive to examine the spectral behavior at Reynolds number larger than the transition Reynolds number, as shown in Fig. 12.

This figure displays energy spectra of the velocity deviation from the laminar flow. The rotation number is fixed
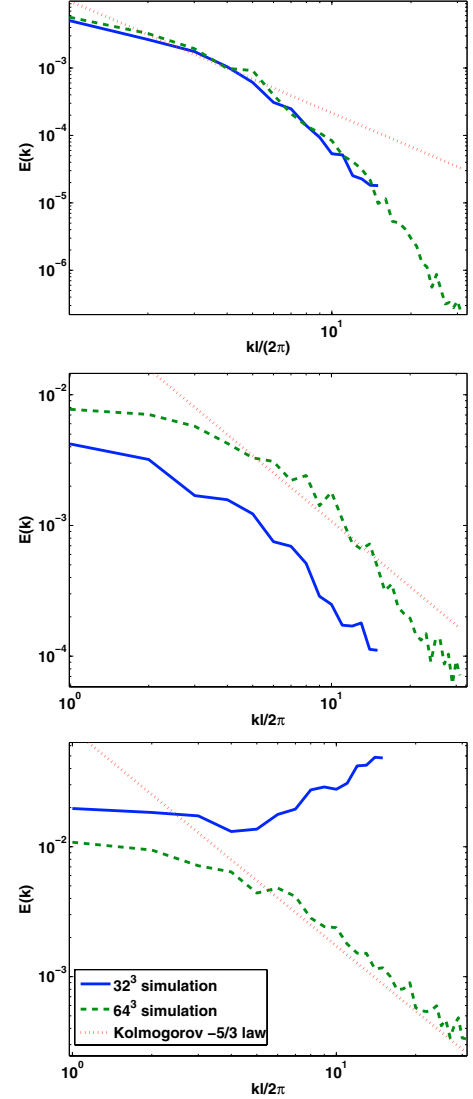
Fig. 12. Energy spectra (of the velocity deviation from the laminar flow), for two different resolutions (32^2 and 64^3). The rotation number is $R_\Omega = -1.016$ in all cases. *Top panel*: Re = 6000. *Middle panel*: Re = 12000. *Bottom panel*: Re = 20 000. At this resolution only the top panel simulations are resolved, as expected. See text for discussion.

at $R_\Omega = -1.016$ for all spectra, and they have been averaged over a 200 shear time period to reduce the noise. From top to bottom, the Reynolds number is 6000, 12 000 and 20 000 respectively. The 32^3 simulations are resolved only in the top panel, while the 64^3 simulations should be resolved in the top two panels. Comparing the second panel with the first reveals a couple of interesting points:

– The 64^3 simulation shows an extension of the spectrum, compatible with a small inertial range (this is difficult to ascertain because of the remaining noise in the simulation), while still resolving at least the top of the dissipation range, but marginally so.

40 G. Lesur and P.-Y. Longaretti: Subcritical turbulence in rotating shear flows
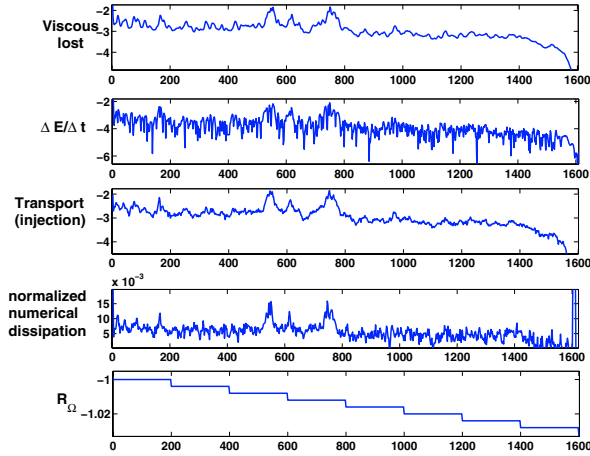
Fig. 13. Energy budget for a 64^3 Re $= 20\,000$ run with our Fourier code. Each plot represent a term in Eq. (8). The numerical dissipation is normalized by the total dissipation $\partial\langle\boldsymbol{w}^2/2\rangle/\partial t - S\langle w_x w_y\rangle$. We find that numerical dissipation is about 1% of the total dissipation. NB: Vertical axis of the three first plots is in logarithmic scale.

– The 32^3 simulation begins to significantly deviate from the 64^3 simulation, although the trend is similar.

The third panel also displays a fairly relevant piece of information. The 64^3 simulation shows both the self-sustaining mechanism scales and the inertial spectra. However, the dissipation scale does not seem to be resolved. This is not unexpected, since increasing the Reynolds number necessarily increases the inertial spectrum, and therefore decreases the dissipation scale. Apparently, the dissipation scale is probably not far off the resolved scales, so that the simulation nevertheless does not noticeably deviate from the expected behavior. But note that the 32^3 simulation is clearly strongly unresolved, with energy accumulating in the small scales in order for a statistically steady equilibrium to be achieved: indeed, as this simulation resolves the self-sustaining mechanism scale, turbulence is present; however, as the smallest resolved scale is significantly larger than the dissipation scale, the spectrum must be strongly deformed to achieve a dissipation which is consistent with the energy input due to the turbulence self-sustaining mechanism.

These simulations illustrate that if the dissipation scale is not resolved, the simulated flow does not necessarily relaminarize, but the deformation of both the amplitude and shape of the spectrum most likely results in, e.g., unreliable estimates of the turbulent transport. In particular, the reliability of finite difference simulations where no viscous term is explicitly included in the code is unclear[15].

On the other hand, this point is related to the fact that the numerical dissipation in a Fourier code is extremely weak, so that the deformation of the spectrum may be quite large. To compute the numerical dissipation explicitly, we have estimated its effect on the turbulent energy budget.

---

[15] We did not further investigate this question here.

We plot an example of such an energy budget in Fig. 13, where all the terms in Eq. (6) are evaluated, so that the remaining difference measures the code dissipation. One should note that these plots are integrated over 2 shear times, so that they include the numerical dissipation due to the desaliazing procedure (done at each time loop) and losses from the remapping procedure (done each shear time). The presented result is generic: for all our simulations, numerical dissipation is found to be at most a few percent of the total dissipation.

In summary, we have tried as much as possible to ensure that our determination of the transition Reynolds number and turbulent transport do not suffer from lack of resolution of the dissipation scale. Note also that the results of the Fourier and finite difference codes are consistent with each other. This makes us confident that our simulations faithfully represent the relevant physics, down to and including the dissipation scale, within the relevant (Re, R_Ω) domain determined at each resolution in Fig. 7.

4.4.3. Shearing sheet simulations and scale invariance

Recently, Balbus (2004) has argued that the scale invariance of the inviscid form of the Navier-Stokes equation used here makes any small scale solution exist at large scales as well. This argument seems to imply that simulations of the kind performed here should not be resolution limited. However, neither the simulations of Balbus et al. (1996), Hawley et al. (1999), the ones performed here, nor a real disk, are scale invariant. In shearing sheet simulations, the box size defines a scale; in a real disk, the disk scale height does. Furthermore, we point out that the mechanism analyzed by Waleffe (1997), whose qualitative and semi-quantitative relevance to the present work has been pointed out hereabove, is somewhat insensitive to the nature of the imposed boundary condition. Along with the results found in this paper, this suggests that only a scale rather than a specific boundary condition needs to be imposed for statistically stationary turbulence to show up in numerical simulations, as exemplified in Sect. 3.4. Finally, the role of an increasingly dominant Coriolis force is not to define another scale, which it cannot, but to modify the relative range of scales that are required for turbulence to exist (most likely because of its more and more stringent time-scale requirement), so that numerical resolution *does* play an important role in subcritical turbulence detection, as can be seen from Fig. 7.

4.5. Boundary conditions and aspect ratio

Assessing the role of boundary conditions on the existence and properties of subcritical turbulence is an important question, since real accretion disk boundary conditions are not reproducible in experimental flows. However, the resolution demand in the local shearing box is already so large for a Keplerian flow that a global simulation of a subcritical Keplerian disk flow is totally out of reach. The best we can do is to compare numerical experiments with shearing sheet and rigid/periodic boundary conditions with one another, and with experimental results. This is the object of this section.
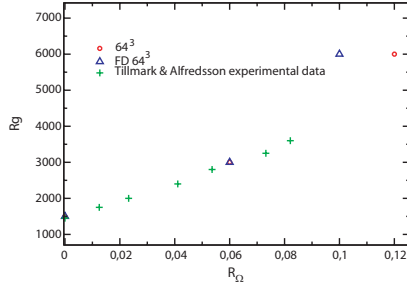
Fig. 14. $Rg(R_\Omega)$ plot from experimental data (Tillmark & Alfredsson 1996, crosses), and our numerical simulations using 64^3 Fourier code (circles) and 64^3 finite difference code (triangles) with cubic box and shearing sheet boundary conditions.

Fig. 15. Re_c as a function of R_Ω for cyclonic rotating plane couette flow.

Before doing so, let us point out some important differences between the two types of boundary conditions:

- In the semi-Lagrangian variables defined by Eqs. (10), the only difference is that the velocity deviation from the laminar flow cancels on the rigid boundary in the rigid/periodic case, while it is periodic in the shear direction (as in the others) in the shearing sheet case. This results in a suppression of the boundary layer in the shearing sheet case.
- Characteristic sizes are the same in both cases. However, while for rigid/periodic conditions, structures are forced to remain more or less stationary with respect to the walls on average, this is not the case with shearing sheet boundary conditions, where structures can move at random through the boundary. As a consequence, a long-lasting mean flow distortion is apparent with rigid/periodic boundary conditions (due to the matching of turbulently enhanced transport with the viscous one in the boundary layer), while in shearing-sheet simulations, although such a distortion is usually locally found at any given time, it averages out over time, due to its random localization.
- This relates to a profound difference between accretion disks and actual experiments. In the latter, the flow profile adjusts to the imposed boundary condition through a pressure redistribution, and a stationary state is reached. In the former, this cannot take place, and the disk is never stationary, due to the resulting turbulent transport of mass and angular momentum.

In spite of these differences, we shall nevertheless argue that the choice of boundary conditions has only a limited impact on some of our qualitative and semi-quantitative results. This suggests that the underlying mechanisms are reasonably closely related in both settings, although much more work than what has been possible to do here is required to ascertain this conclusion.

4.5.1. Cyclonic rotation

Figure 14 displays a comparison of our numerical results with the Tillmark & Alfredsson (1996) data, in the range of rotation number where these data were collected.

The agreement between the two is fair, with the Fourier code results being sensibly more compatible with the data than the finite difference code ones, at the larger rotation numbers. This follows because, at the same "resolution", a Fourier code is physically more resolved than a Finite difference code. Note also that some 128^3 simulations were performed using the Fourier code and the same transition thresholds were found as for the 64^3 simulations. This supports the idea that the 64^3 Fourier code results are not resolution limited.
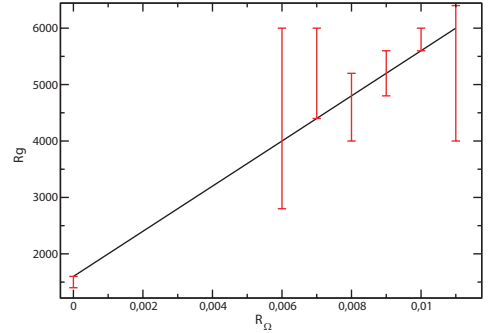
We have also made a few runs using rigid (shearwise direction) and periodic (other directions) boundary conditions with our ZEUS-like code. At each rotation number, we made a few tries with different Reynolds numbers to locate the transition threshold. Each run was computed from the same initial condition for 400 shear times with $80 \times 80 \times 40$ grid points and a $L_x = 1.75\pi\, L_y = 1\, L_z = 1.2\pi$ aspect ratio box (corresponding to the "minimal flow unit" aspect ratio, i.e. the smallest box in which turbulence can be sustained with these boundary conditions: see Hamilton et al. 1995, for details). The error bars upper bounds correspond to the lower Reynolds for which turbulence is found and the lower bound the higher Reynolds number for which turbulence is lost. The numerical data are shown in Fig. 15; the error bars reflect our poor sampling, not intrinsic fluctuations in the transition Reynolds number. These data are fitted by a linear law:

$$Rg = 1400 + 4 \times 10^5 R_\Omega, \tag{32}$$

the slope of which is 15 times steeper than the one found from the experimental data.

This dramatic difference in transition Reynolds number with respect to the experimental and shearing sheet results is in fact controlled by the choice of the simulation box aspect ratio. For example, let us choose a longer box in the z direction (i.e. $L_x = 1.75\pi\, L_y = 1\, L_z = 2.4\pi$). With such a choice, turbulence is sustained at $R_\Omega = 0.01$ and Re = 2400, much closer to the expected transition Reynolds of Fig. 14 than what is predicted by Fig. 15. Finally, Komminaho et al. (1996), using a very elongated simulation box in the flow direction, found transition right at the experimentaly determined Reynolds number ($Rg = 3000$, $R_\Omega = 0.06$).

These result show the important role of aspect ratio in subcritical turbulence simulations with rigid/periodic boundary conditions. Apparently, the use of shearing sheet boundary conditions relaxes this constraint. This is reasonable since the

42   G. Lesur and P.-Y. Longaretti: Subcritical turbulence in rotating shear flows
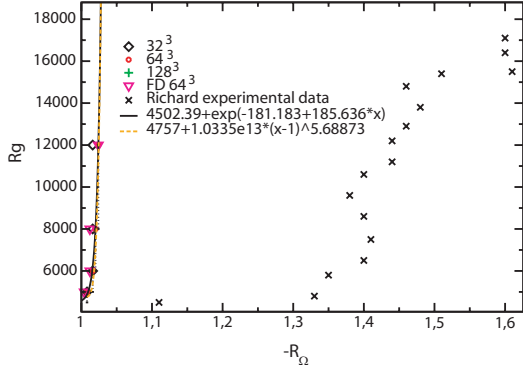
Fig. 16. $Rg(R_\Omega)$ plot from experimental data on Taylor-Couette flows (Richard 2001, crosses), and the various numerical simulations results and related fits shown in Fig. 7.

shearing sheet box allows more freedom than rigid boundary conditions. In actual experiments, the aspect ratio is not an issue since usually very large L_x/L_y and L_z/l_y are used, so that the turbulence coherence length can freely adjust itself in these directions.

These results also indirectly suggest that the turbulence saturation mechanism is not strongly affected by the use of shearing sheet boundary conditions. One would nevertheless expect that the reduction of the shear in the middle of the flow, due to the mean velocity profile modification which occurs with rigid/periodic boundary conditions, produces a reduced turbulent transport. This is indeed the case: e.g., the turbulent transport at marginal stability ($R_\Omega = 0$) is $\langle v_x v_y \rangle \simeq 2 \times 10^{-3} (S d)^2$ for the rigid/periodic boundary conditions[16], while one has $\langle v_x v_y \rangle \simeq 0.4 (S d)^2$ throughout the flow with the shearing sheet boundary conditions, although the transition Reynolds number is the same in both instances. These features most probably find a natural explanation if the turbulence amplitude saturation mechanism is primarily controlled by the system nonlinearities, and not by the mean profile deformation.

4.5.2. Anticyclonic rotation

The comparison of our numerical results with Richard (2001) data is shown in Fig. 16.

The discrepancy between the experimental and numerical data is striking, especially at the light of the remarkable consistency observed for cyclonically rotating flows. In particular, the increase in transition Reynolds is considerably steeper in the numerical data than in the experimental ones. Note however that the numerical and experimental data seem to give the same transition Reynolds number *at the marginal stability boundary*.

Longaretti & Dauchot (2005) have argued that the flow curvature plays no role in the anticyclonic flow data of Richard (2001), so that the origin of the large discrepancy between the

numerical and experimental results must be found elsewhere[17]. In this respect, note that experimental secondary flow distortions are much more likely to induce a linear instability somewhere in the flow on the anticyclonic side as on the cyclonic one. Indeed, recall that the stability limit is defined by Eq. (9). Consider the cyclonic marginal stability limit first ($R_\Omega = 0$), and assume that one moves away from it by imposing a small change in rotation $\delta\Omega$. The required change in shear profile δS to locally achieve $2\delta\Omega/(S(y) + \delta S) < 0$ is large: $\delta S \sim S(y)$ is needed. Conversely, at the anticyclonic marginal stability limit ($R_\Omega = -1$, i.e., $S = 2\Omega$), upon a small change $\delta\Omega$ of the rotation rate, a change $\delta S \simeq 2\delta\Omega \ll S$ suffices to locally make $2\Omega/S > -1$ and produce a linear instability somewhere in the system. This argument shows that the presence of secondary flows, such as Ekmann's circulation, can easily make the flow more unstable than it would be in its absence in anticyclonic flows, whereas this is much more difficult to achieve in cyclonic ones. This may easily explain the discrepancy between numerical and experimental results shown in Fig. 16, while the agreement is remarkable at the marginal stability boundary.

5. Summary and conclusions

The central results of this paper are displayed in Figs. 4, 5, 7−9, and their significance and implications are discussed in Sects. 3.3, 3.4, 4.1−4.4. The main implications of these results are summarized in the abstract. In the course of the discussion, we have found that a number incorrect statements have been made in the literature, most notably concerning the existence and importance of subcritical turbulence in presence of a dynamically significant Coriolis force. We have also found that resolution is a key issue for subcritical anticyclonically rotating flows (including Keplerian ones), and have quantified the relation between resolution, rotation and Reynolds number. In relation to this, we believe that the question of resolution of the dissipation scale is not emphasized enough in the astrophysics literature, and the potential effects of this problem are most probably underestimated.

Our simulations do not faithfully represent a real disk: neither vertical stratification, nor, more critically, realistic vertical boundary conditions have been implemented. A real (hydrodynamic disk) moves either in vacuum, or, more probably, in a hot corona. In both cases, one expects the real vertical boundary condition in the disk to be (nearly) stress-free. We have made some very preliminary simulations of ah stratified disk-corona system to test this idea, where most of the inertia lies in the disk. Although a strong numerical mixing of the corona and the disk at the interface prevents us to evolve the system for a long time ($50t_s$ max), no significant difference in the overall dynamics of the disk did show up. However this problem probably requires more careful investigations to validate this conclusion.

Overall, the outcome of this investigation still leaves us with the issue of transport unresolved in MHD-inactive flows

---

[16] This is measured in the middle of the flow where the turbulent transport is maximized, and viscous transport negligible.

[17] In any case, the flow curvature always increases the transition Reynolds number, so that including curvature in the analysis of this problem can only make it worse, not better.

(and possibly in some MHD-active ones), and we will briefly comment the various ways out of this conundrum.

We first note that an efficient enough local instability should lead to a large enough turbulent transport, because the transition to fully developed turbulence usually occurs to significantly lower Reynolds numbers in these systems than the ones found here. This is true, e.g., in rotating shear flows of the type considered here, in the linearly unstable regime. However, no such instability has yet been found in hydrodynamical Keplerian flows, either stratified or not, as discussed in the introduction. It remains to be seen whether another such instability can operate in hydrodynamic disks, but the list of potential driving agents has by now significantly been narrowed.

In what concerns the YSO disks dead-zone in particular, it may be that the disk stirring due to the MRI above and below the dead-zone itself (Fleming & Stone 2003) might provide enough transport in the end if it excites large enough large scale 2D disturbances of the right type (Ioannou & Kakouris 2001) in the disk. However, this option remains to be worked out in detail.

It has often been noted that transport in disks may not be due to turbulence but to waves (see, e.g., Papaloizou & Lin 1995 for an introduction to the subject). Recent results on the existence of vortices in stratified disks (Barranco & Marcus 2005) and on the coupling of waves to vortices resulting in efficient transport in 2D dynamics (Bodo et al. 2005 and references therein) support this idea.

Appendix A: Displaced particle analysis for rotating flows

The following line of argument closely follows Tritton & Davies (1981) and Tritton (1992). Let us consider a rotating shear flow, whose dynamics is controlled by Eq. (1). As in Sect. 2.1, x is the direction of the flow, y the direction of the shear, and z the direction perpendicular to the x, y plane, in which the rotation $\boldsymbol{\Omega}$ is applied. The laminar equilibrium velocity $\boldsymbol{u}_L = (U(y), 0, 0)$ generates a Coriolis force in the y direction of magnitude $-2\rho\Omega U$ (in algebraic value), which is balanced by the equilibrium generalized pressure gradient $-\mathrm{d}\pi/\mathrm{d}y$.

Let us further consider two fluid "rods" of infinite extent in the streamwise direction x, and located at positions y_1 and $y_2 = y_1 + \delta y$. The streamwise velocities of these rods are U_1 and U_2, respectively. Let us assume that one displaces the rod at y_1 to location y_2, without disturbing the pressure distribution. Although the total work of the Coriolis force vanishes, there is a net partial work due to the force component in the x direction which originates in the velocity v of this displacement in the y direction. Because of this partial work, the rod experiences a change of x momentum, and therefore of x velocity, which reads

$$U_1' - U_1 = \int 2\Omega v \mathrm{d}t = 2\Omega \delta y, \qquad (A.1)$$

so that the velocity U_1' of the rod when it reaches location y_2 differs from the equilibrium velocity U_2, and correlatively, the x component of the Coriolis force acting on this displaced
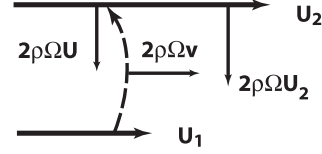

Fig. A.1. Sketch of the effect of the Coriolis force on the displaced particle (see text).

rod, $-2\rho\Omega U_1'$ (in algebraic value) differs from the equilibrium one, $-2\rho\Omega U_2$ (see Fig. A.1).

Consequently, the net result between the equilibrium pressure gradient and the Coriolis force will tend to restore the displaced rod to its equilibrium position[18] if $U_1' > U_2$, or displace it further if $U_1' < U_2$. From Eqs. (A.1) and (3), one obtains

$$U_1' - U_2 = 2\Omega \delta y - \frac{\mathrm{d}U}{\mathrm{d}y}\delta y = S(R_\Omega + 1)\delta y, \qquad (A.2)$$

where $S = -\mathrm{d}U/\mathrm{d}y$ is the shear. From this result, the net force (Coriolis and pressure) on the displaced rod reads

$$2\rho\Omega(U_2 - U_1') = -\rho S^2 R_\Omega(R_\Omega + 1)\delta y. \qquad (A.3)$$

This shows that equilibrium is always restored when $R_\Omega > 0$ or $R_\Omega < -1$ and destroyed otherwise (equality holds at marginal stability). This is the result quoted in Sect. 2.1. This result can also be directly derived from the linearized eulerian equation of motion with the use of spatially uniform perturbations of the pressure and the velocity.

References

Afshordi, N., Mukhopadhyay, B., & Narayan, R. 2005, ApJ, 629, 373
Arlt, R., & Urpin, V. 2004, A&A, 426, 755
Balbus, S. A. 2003, ARA&A, 41, 555
Balbus, S. A. 2004, A&A, submitted [arXiv:astro-ph/0408510]
Balbus, S. A., & Hawley, J. F. 1991, ApJ, 376, 214
Balbus, S. A., Hawley, J. F., & Stone, J. M. 1996, ApJ, 467, 76
Barranco, J. A., & Marcus, P. S. 2005, ApJ, 623, 1157

[18] Consider the direction and magnitude of the Coriolis force and pressure force along the y axis to derive the effect of the inequality.

44   G. Lesur and P.-Y. Longaretti: Subcritical turbulence in rotating shear flows

Bech, K. H., & Andersson, H. I. 1997, J. Fluid Mech., 347, 289

Blaes, O. M. 1987, MNRAS, 227, 975

Bodo, G., Chagelishvili, G., Murante, G., et al. 2005, A&A, 437, 9

Bottin, S., Dauchot, O., & Daviaud, F. 1997, Phys. Rev. Lett., 79, 4377

Brandenburg, A., & Dintrans, B. 2001 [arXiv:astro-ph/0111313]

Brosa, U., & Grossmann, S. 1999, European Phys. J. B, 9, 343

Cabot, W. 1996, ApJ, 465, 874

Cambon, C., Benoit, J., Shao, L., & Jacquin, L. 1994, J. Fluid Mech., 278, 175

Chagelishvili, G. D., Zahn, J.-P., Tevzadze, A. G., & Lominadze, J. G. 2003, A&A, 402, 401

Darbyshire, A. G., & Mullin, T. 1995, J. Fluid Mech., 289, 83

Dauchot, O., & Daviaud, F. 1995a, Phys. Fluids, 7, 335

Dauchot, O., & Daviaud, F. 1995b, Phys. Fluids, 7, 901

Daviaud, F., Hegseth, J., & Bergé, P. 1992, Phys. Rev. Lett., 69, 2511

Drazin, P., & Reid, W. 1981, Hydrodynamic stability (Cambridge Univ. Press)

Dubrulle, B. 1993, Icarus, 106, 59

Dubrulle, B., & Zahn, J.-P. 1991, J. Fluid Mech., 231, 561

Dubrulle, B., Dauchot, O., Daviaud, F., et al. 2005a, Phys. Fluids, accepted

Dubrulle, B., Marié, L., Normand, C., et al. 2005b, A&A, 429, 1

Eckhardt, B., & Mersmann, A. 1999, Phys. Rev. E, 60, 509

Faisst, H., & Eckhardt, B. 2004, J. Fluid Mech., 504, 343

Fleming, T., & Stone, J. M. 2003, ApJ, 585, 908

Gammie, C. F. 1996, ApJ, 457, 355

Garaud, P., & Ogilvie, G. I. 2005, J. Fluid Mech., submitted [arXiv:astro-ph/0503223]

Goldreich, P., & Schubert, G. 1967, ApJ, 150, 571

Goodman, J., & Balbus, S. A. 2001 [arXiv:astro-ph/0110229]

Grossman, S. 2000, Rev. Mod. Phys., 72, 603

Hamilton, J. M., Kim, J., & Waleffe, F. 1995, J. Fluid Mech., 287, 317

Hawley, J. F. 1991, ApJ, 381, 496

Hawley, J. F., Balbus, S. A., & Winters, W. F. 1999, ApJ, 518, 394

Hawley, J. F., Gammie, C. F., & Balbus, S. A. 1995, ApJ, 440, 742

Hersant, F., Dubrulle, B., & Huré, J.-M. 2005, A&A, 429, 531

Ioannou, P. J., & Kakouris, A. 2001, ApJ, 550, 931

Johnson, B. M., & Gammie, C. F. 2005a, ApJ, 626, 978

Johnson, B. M., & Gammie, C. F. 2005b, in preparation

Klahr, H. 2004, ApJ, 606, 1070

Klahr, H. H., & Bodenheimer, P. 2003, ApJ, 582, 869

Komminaho, J., Lundbladh, A., & Johansson, A. V. 1996, J. Fluid Mech., 320, 259

Leblanc, S., & Cambon, C. 1997, Phys. Fluids, 9, 1307

Lerner, J., & Knobloch, E. 1988, J. Fluid Mech., 189, 117

Lesieur, M. 1990, Turbulence in fluids third edition (Kluwer)

Longaretti, P.-Y. 2002, ApJ, 576, 587

Longaretti, P.-Y., & Dauchot, O. 2005, in Proc. Bristol 2004 Symposium on the laminar-turbulent transition, ed. Kerswell & Mullin (Kluwer)

Mukhopadhyay, B., Afshordi, N., & Narayan, R. 2005, ApJ, 629, 383

Ogilvie, G. I. 2003, MNRAS, 340, 969

Papaloizou, J. C. B., & Lin, D. N. C. 1995, ARA&A, 33, 505

Papaloizou, J. C. B., & Pringle, J. E. 1984, MNRAS, 208, 721

Pedley, T. J. 1969, J. Fluid Mech., 35, 97

Peyret, R. 2002, Spectral Methods for Incompressible Viscous Flow (Springer)

Pumir, A. 1996, Phys. Fluids, 8, 3112

Rüdiger, G., Arlt, R., & Shalybkov, D. 2002, A&A, 391, 781

Richard, D. 2001, Ph.D. Thesis, Université de Paris VII

Richard, D., & Zahn, J. 1999, A&A, 347, 734

Richard, D., Dauchot, O., & Zahn, J.-P. 2001, in Proc. of the 12th Couette-Taylor Workshop, Evanston, USA

Rogallo, R. S. 1981, NASA STI/Recon Technical Report N, 81, 31508

Romanov, V. A. 1973, Func. Anal. Appl., 7, 137

Salhi, A., & Cambon, C. 1997, J. Fluid Mech., 347, 171

Satomura, T. 1981, J. Meteor. Soc. Japan, 59, 148

Schmiegel, A., & Eckhardt, B. 1997, Phys. Rev. Lett., 79, 5250

Shakura, N. I., Sunyaev, R. A., & Zilitinkevich, S. S. 1978, A&A, 62, 179

Shalybkov, D., & Ruediger, G. 2005, A&A, 438, 411

Sipp, D., & Jacquin, L. 2000, Phys. Fluids, 12, 1740

Speziale, C. G. 1991, Ann. Rev. Fluid Mech., 23, 107

Speziale, C. G., & Mhuiris, N. M. 1989, Phys. Fluids, 1, 294

Stone, J. M., & Balbus, S. A. 1996, ApJ, 464, 364

Stone, J. M., & Norman, M. L. 1992, ApJS, 80, 753

Taylor, G. I. 1936, Proc. Roy. Soc. London A, 157, 546

Tevzadze, A. G., Chagelishvili, G. D., Zahn, J.-P., Chanishvili, R. G., & Lominadze, J. G. 2003, A&A, 407, 779

Tillmark, N., & Alfredsson, P. H. 1996, in Advances in Turbulence VI., ed. S. Gavrilakis, L. Machiels, & P. A. Monkewitz (Kluwer), 391

Tritton, D. J. 1992, J. Fluid Mech., 241, 503

Tritton, D. J., & Davies, P. A. 1981, in Hydrodynamic instabilities and the transition to turbulence (Springer-Verlag), 229

Umurhan, O. M. 2005, MNRAS, submitted [arXiv:astro-ph/0506016]

Umurhan, O. M., & Regev, O. 2004, A&A, 427, 855

Urpin, V. 2003, A&A, 404, 397

Waleffe, F. 1995, Phys. Fluids, 7, 3060

Waleffe, F. 1997, Phys. Fluids, 9, 883

Waleffe, F. 2003, Phys. Fluids, 15, 1517

Wendt, G. 1933, Ing. Arch., 4, 577

Yecko, P. A. 2004, A&A, 425, 385

2. Impact of dimentionless numbers on the efficiency of MRI-Induced turbulent transport

Impact of dimensionless numbers on the efficiency MRI-induced turbulent transport.

Lesur, G.[1] and P-Y. Longaretti[1]

[1] *Laboratoire d'Astrophysique Observatoire de Grenoble*
BP 53, 38041 GRENOBLE CEDEX 9

ABSTRACT

The magneto-rotational instability is presently the most promising source of turbulent transport in accretion disks. However, some important issues still need to be addressed to quantify the role of MRI in disks; in particular no systematic investigation of the role of the physical dimensionless parameters of the problem on the dimensionless transport has been undertaken yet. After generalizing existing results on the marginal stability limit in presence of both viscous and resistive dissipation, we reexamine this problem through numerical simulations in the simplest setting of a local, unstratified shearing box, with the help of a pseudo spectral incompressible 3D code; viscosity and resistivity are explicitly accounted for. We focus on the effect of the dimensionless magnetic field strength, the Reynolds number, and the magnetic Prandtl number. First, we complete existing investigations on the field strength dependence by showing that the transport in high magnetic pressure disks close to marginal stability is highly time-dependent and surprisingly efficient. Second, we bring to light a significant dependence of the global transport on the magnetic Prandtl number, with $\alpha \propto Pm^{\delta}$ for $0.12 < Pm < 8$ and $200 < Re < 6400$ (δ being in the range 0.25 to 0.5), which is not correlated to the linear growth rate. This result is quite critical to accretion disk transport theory, as the magnetic Prandtl number Pm is expected to vary by many orders of magnitude between the various classes of disks, from $Pm \ll 1$ in YSO disks to $Pm \gg 1$ in AGN disks. More generally, these results stress the need to control dissipation processes in astrophysical simulations.

1 INTRODUCTION

Angular momentum transport has always been a central issue in accretion disk theory. The first α model (Shakura & Sunyaev 1973) already assumed the presence of strong turbulent motions, modelled through an effective viscosity, orders of magnitude larger than the expected disk molecular viscosity. Since then, the physical origin of this turbulence has been highly debated. As purely hydrodynamic non stratified Keplerian flows are known to be linearly stable to small perturbations, a finite amplitude instability was first envisioned to trigger turbulence. This question was studied both experimentally (Richard & Zahn 1999; Richard 2001; Richard et al. 2001) and numerically (Balbus et al. 1996; Hawley et al. 1999), leading to a long controversy. More recent numerical and experimental investigations of this problem strongly support the idea that the transport due to this mechanism, if present, would be far too inefficient to account for the short disk evolution time-scales imposed by astrophysical observations (Lesur & Longaretti 2005; Ji et al. 2006). Linear instabilities of hydrodynamic origin have also been envisioned as a source of turbulence, relating in particular to the flow stratification (Klahr & Bodenheimer 2003; Urpin 2003; Dubrulle et al. 2005; Shalybkov & Ruediger 2005), but these are either not present or too inefficient

(Johnson & Gammie 2006; Arlt & Urpin 2004; Longaretti & Lesur 2007; see Lesur & Longaretti 2005 and references therein for a recent review of this issue).

The potential role of MHD instabilities in accretion disks was pointed out in a seminal paper by Balbus & Hawley (1991), devoted to an analysis of what is now known as the magneto-rotational instability (MRI). This instability has been extensively studied since then, mainly with the help of local (Hawley et al. 1995; Stone et al. 1996) and global (Hawley 2000) 3D numerical simulations. Although a more recent set of numerical simulations did focus on MRI energetics (Gardiner & Stone 2005), the dissipation of turbulent fields in these simulations is not controlled, as no physical term was introduced to account for physical viscosity and resistivity. Note however that Brandenburg et al. (1995) have introduced such dissipation in their simulations, but kept it as small as possible, leading to simulations dominated by artificial and numerical dissipations. The resistive term alone has also been introduced by Fleming et al. (2000), but viscous effects were still neglected. This raises questions about the exact role of numerical dissipation in all these simulations, especially at the light of our recent investigation of subcritical turbulence in accretion disks (Lesur & Longaretti 2005), which clearly showed that a careful con-

2   *Lesur, G. and P-Y. Longaretti*

trol of dissipation and resolution — and more generally of the dimensionless parameters of the problem — is required to properly quantify turbulent transport.

This issue is addressed here in the context of MRI-driven turbulence, using a 3D spectral Fourier code, which allows a precise monitoring of viscous, resistive and numerical dissipation. First, we recall the MHD equations in the shearing sheet framework (Hawley et al. 1995), along with the relevant dimensionless parameters of the problem, and summarize what is known about their effect on MRI-induced turbulent transport. Next, we investigate the linear stability of the MRI, which to the best of our knowledge has not been characterized when both viscosity and resistivity are accounted for in the dispersion relation. Then, we present new results on the behavior of turbulent transport in dimensionless parameters regime that have not been investigated in the past: first, very close to the threshold of instability (in terms of relative magnetic field strength), and then with respect to the magnetic Prandtl number, which has been ignored in all previous investigations. The dependence of turbulence transport on the magnetic Prandtl number is the most significant finding of this investigation. This dependence may turn out to be critical, as the magnetic Prandtl number varies by many order of magnitudes in astrophysical disks. The astrophysical implications of our findings are further discussed in our concluding section, and potential caveats relating to numerical limitations that may influence our results.

2   SHEARING BOX CHARACTERIZATION AND SUMMARY OF EARLIER RESULTS

The MRI has already been extensively studied in the literature (see, e.g., Balbus 2003 and references therein for a review of the subject). Our objective is to extend previous work through a systematic exploration of the dependence of the MRI-induced transport on the physical quantities characterizing the problem. For simplicity, we work in a shearing sheet setting (see Hawley et al. 1995 for a description of the shearing box equations, numerical boundary conditions, and conserved quantities); vertical stratification is ignored, but both viscous and resistive microphysical (molecular) dissipation are included. This differs from previous investigations, where this is always ignored. Our previous experience with subcritical hydrodynamic transport has shown us that the inclusion of explicit dissipation is required to precisely characterize transport properties and distinguishing resolved simulations from unresolved ones (see Lesur & Longaretti 2005 for an extensive discussion and illustration of these points).

The problem is formulated in a cartesian frame centered at $r = R_0$, rotating with the disk at $\Omega = \Omega(R_0)$ with radial dimension $H \ll R_0$. In this work, H is the size of our simulation boxes, in all spatial dimensions. This leads to the following set of equation, assuming $\phi \to x$, $r \to -y$:

$$\partial_t \boldsymbol{u} + \boldsymbol{u} \cdot \boldsymbol{\nabla} \boldsymbol{u} = -\frac{1}{\rho}\boldsymbol{\nabla}P + \frac{1}{\mu_0\rho}(\boldsymbol{\nabla} \times \boldsymbol{B}) \times \boldsymbol{B}, \tag{1}$$
$$-2\boldsymbol{\Omega} \times \boldsymbol{u} - 2\Omega Sy\boldsymbol{e_y} + \nu\boldsymbol{\Delta}\boldsymbol{u}$$
$$\partial_t \boldsymbol{B} = \boldsymbol{\nabla} \times (\boldsymbol{u} \times \boldsymbol{B}) + \eta\boldsymbol{\Delta}\boldsymbol{B}, \tag{2}$$
$$\nabla \cdot \boldsymbol{u} = 0, \tag{3}$$
$$\nabla \cdot \boldsymbol{B} = 0, \tag{4}$$

where the medium shear is defined by $S = -r\partial_r\Omega$. For simplicity, incompressible motions are assumed. This is a priori justified by the fact that MRI-induced motions are usually subsonic, so that one expects at least in first approximation that compressibility effects do not play a major role in the problem. This approximation allows us to remove the flow Mach number from the list of dimensionless parameters characterizing the problem, so that we can more effectively isolate and quantify the role of the various physical agentsh.

The terms on the right-hand side member of Eq. (1) are the gas pressure, Lorentz force, Coriolis force, tidal force, and viscous dissipation, respectively. The steady-state solution to this equation is the local profile $\boldsymbol{u} = Sy\boldsymbol{e_x}$ with $S = 3/2\Omega$ for Keplerian disks. In the remainder of this paper, we will use the deviation from the laminar profile $\boldsymbol{v}$ defined by $\boldsymbol{v} = \boldsymbol{u} - Sy\boldsymbol{e_x}$. For simplicity, we take the steady-state magnetic field B_0 along the vertical axis. Note that this field is also the average field in the shearing sheet box, and is conserved during the evolution thanks to the shearing sheet boundary conditions (Hawley et al. 1995).

These equations are characterized by four dimensionless numbers, the first three relating to the Navier-Stokes equation while the last one belongs to the induction equation:

• The Reynolds number, $Re \equiv SH^2/\nu$, measuring the relative importance of nonlinear coupling through the advection term, and viscous dissipation.
• A proxy to the plasma beta parameter, defined here as $\beta = S^2 H^2/V_A^2$ where $V_A^2 = B_o^2/\mu_o\rho$ is the Alfvén speed. The rationale of this definition follows from the vertical hydrostatic equilibrium constraint $c_s \sim \Omega H$, which is expected to hold in thin disks, so that our definition of β is indeed related to the plasma parameter in an equivalent, vertically stratified disk. This parameter measures the relative weight of the Lorentz force and the advection term.
• The rotation number (inverse Rossby number), defined as $R_\Omega = 2\Omega/S$, which measures the relative importance of the Coriolis force.
• The magnetic Reynolds number, $R_m = SH^2/\eta$, which measures the relative importance of resistive dissipation with respect to the ideal term in the induction equation.

We consider only Keplerian disks in this investigation, so that the rotation number is held fixed to its Keplerian value $R_\Omega = -4/3$. This leaves us with three independent dimensionless numbers: β, Re, and Rm.

On the other hand, the (local in the disk) dimensionless transport coefficient,

$$\alpha = \frac{\langle v_x v_y - B_x B_y/(\mu_o\rho)\rangle}{S^2 H^2}, \tag{5}$$

being a dimensionless number, can only depend on the local dimensionless parameters characterizing the flow that we have just defined (the bracketing refers to appropriate

Impact of dimensionless numbers on the efficiency MRI-induced turbulent transport. 3

box and/or time averages) [1]. Our task reduces to characterize this dimensionless transport, as a function of the three independent dimensionless numbers just defined. However, for later convenience, we take them to be β, Re and $P_m \equiv \nu/\eta = Rm/Re$ instead (the rationale of this latter choice will become apparent later on).

All previous investigations ignore the dependence on the last two dimensionless numbers, who have not been included in the physical description up to now. Within such an approximation, Hawley et al. (1995) have characterized the dependence of α on β. Their results imply that

$$\alpha \simeq 3\beta^{-1/2}, \qquad (6)$$

from their Eqs. (10), (15), (16) and (18).

This implies in particular that α increases when the initial (and box average) magnetic field B_o is increased. However, for a large enough field, the smallest unstable wavelength (which increases along with B_o) becomes larger than the box size, and the instability is quenched. On this basis, one expects that the scaling Eq. (6) would break down close enough to the critical β stability limit. This question is somewhat investigated in the present work. However, most of our effort is devoted to characterizing the Re and Pm dependence of α.

3 LINEAR STABILITY ANALYSIS

The linear stability of differentially rotating disks in presence of a magnetic field was first investigated in the astrophysical context by Balbus & Hawley (1991). Then, the instability in the weakly ionized case has been considered (Blaes & Balbus 1994; Wardle 1999; Balbus & Terquem 2001), leading to the well known Dead Zone problem (Gammie 1996). However, we are not aware of any clear indication of the stability limits of the fluid when both viscous and resistive dissipation are present in the general astrophysical context. Some discussions has been done on this point in the litterature, mostly motivated by liquid-metal experiments, in the limit $Pm \ll 1$ (Ji et al. 2001; Rüdiger & Shalybkov 2002). However, these papers exhibit no clear asymptotical limit that may be applied for astrophysical disks. Therefore, we provide such an analysis here, as a prelude to our nonlinear simulations.

We will consider only axisymmetric perturbations, so that we can eliminate the azimuthal perturbation transport term. Note that this assumption does not seem to have a great influence on the stability limit, since 3D numerical simulations and linear analysis of axisymmetric modes exhibit nearly the same stability limit; this holds in particular in the simulations presented here. The new physics introduced by these equations is the ν and η coefficient, which are respectively the kinematic viscosity and resistivity.

We linearize and Fourier transform the equations of motion by assuming $\boldsymbol{v} = \boldsymbol{v_0}\exp\big(i(\omega t - k_y y - k_z z)\big)$ and $\boldsymbol{b} = \boldsymbol{b_0}\exp\big(i(\omega t - k_y y - k_z z)\big)$. This yields the following linearized equation set:

[1] It may also depend on the simulation aspect ratio and resolution, from a numerical point of view.

$$
\begin{aligned}
(i\omega + \nu k^2)\boldsymbol{v_0} &= i\,\boldsymbol{k}\psi - i\,k_z\frac{B_0}{\mu_0\rho_0}\boldsymbol{b_0} & (7) \\
&\quad + (2\Omega - S)v_y\boldsymbol{e_x} - 2\Omega v_x\boldsymbol{e_y}, \\
(i\omega + \eta k^2)\boldsymbol{b_0} &= -i\,k_z B_0\boldsymbol{v} + b_y S\boldsymbol{e_x}, & (8) \\
i\,\boldsymbol{k}\cdot\boldsymbol{v} &= 0, & (9) \\
i\,\boldsymbol{k}\cdot\boldsymbol{B} &= 0, & (10)
\end{aligned}
$$

where ψ is the perturbation in total pressure $(P + B^2/\mu_0)/\rho$. Introducing $\omega_\nu \equiv \omega - i\nu k^2$ and $\omega_\eta \equiv \omega - i\eta k^2$, the Alfvén speed $V_A^2 = B_0^2/\mu_0\rho$, the epicyclic frequency $\kappa^2 = 2\Omega(2\Omega - S)$ and $\gamma^2 = k_z^2/k^2$, one eventually gets the dispersion relation:

$$
\begin{aligned}
(\omega_\nu\omega_\eta - k_z^2 V_A^2)\Big(&\omega_\nu^2\omega_\eta^2 - 2\omega_\nu\omega_\eta k_z^2 V_A^2 - \omega_\eta^2\kappa^2\gamma^2 \\
&- k_z^2 V_A^2\big(2\Omega S\gamma^2 - k_z^2 V_A^2\big)\Big) = 0. \quad (11)
\end{aligned}
$$

which we now solve in various dissipation regimes.

3.1 $Pm = 1$ behavior

Let us first look at the $Pm = 1$ case, where the dispersion equation can be solved exactly by analytical means. The condition $\Im(\omega) < 0$ expresses the existence of the instability. From this condition, the MRI exists if and only if $\nu^2 k^4 < -\omega_\nu^2$. From this constraint and the dispersion relation Eq. (11), one find that:

$$\nu^2 < \frac{\sqrt{\kappa^4\gamma^4 + 16k_z^2 V_A^2\Omega^2\gamma^2}}{2k^4} - \frac{k_z^2 V_A^2}{k^4} - \frac{\kappa^2\gamma^2}{2k^4}, \qquad (12)$$

is a necessary and sufficient criterion for instability. One can check that the highest ν values obtain when $\gamma = 1$ and $k_z = \min(k_z) = 2\pi/H$, which corresponds to the so-called channel flow solution in the z direction. From our definition of the Reynolds number as $Re = SH^2/\nu$ where H is the numerical box height or the typical disk height, and of the plasma parameter $\beta = S^2 H^2/V_A^2$, the stability limit Eq. (12) translates into a relation between these two parameters, represented on Fig. 1.

Note that the instability has two different limits, depending on the β parameter:

• A high β regime, corresponding to a low magnetic pressure. In this regime, marginal stability occurs at a characteristic Reynolds number value $Re_c \simeq 80$. This behavior illustrates that the growth time scale of the most unstable mode must be shorter than the dissipation time scale, defined by $\tau_d \simeq k^2/\nu$.

• A low β regime, which is nearly Reynolds independent. In this region, one can define a critical β ($\beta_c = 29.5$) for which the MRI is lost. This behavior can be explained by considering the unstable mode of shortest wavelength: as β goes to smaller values, the smallest unstable wavelength increases (see Eq. 12). At some point it becomes larger than the scale height H (or box size in our case) and the instability is lost. Since this phenomenon takes place at large scale, the Reynolds number has naturally no role to play in it. Note that this regime is not specific to our unstratified
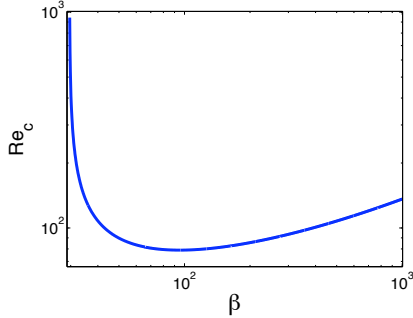
Figure 1. MRI linear stability limit

calculation, since similar results are found for a stratified medium where marginal stability usually occurs for $\beta_c \gtrsim 1$ (see e.g Balbus & Hawley 1991 and Gammie & Balbus 1994). This limit is reached when the last factor in Eq. (11) cancels out, i.e., when $2\Omega S = V_A^2 k_z^2$ (the usual dissipationless MRI stability limit).

3.2 $Pm \neq 1$ behavior

The dispersion relation can no longer be solved exactly in this case, but an approximate solution can be found in the low magnetic field limit ($V_A \to 0$, or more precisely $V_A k_z \ll \kappa$), where marginal stability follows from a balance between the destabilizing term, and the dissipation ones. The "opposite" (high β) marginal stability limit, where destabilization is balanced by the usual Alfvénic magnetic tension, is briefly addressed at the end of this section.

In the limit of vanishing magnetic field, the dispersion relation has two relevant roots $\omega_\eta^2 = 0$ and $\omega_\nu^2 = \kappa^2$. In what follows, we refer to these roots as the Alfvénic and the inertial branch, respectively. Looking for the first order correction in $V_A^2 k_z^2$ to the Alfvénic branch yields the following result, which describes the MRI modes:

$$\omega = i\eta k_z^2 \pm i \left(\frac{2\Omega S}{k_z^4(\eta-\nu)^2 + \kappa^2} \right)^{1/2} V_A k_z. \qquad (13)$$

Note that viscosity and resistivity do not play a symmetric role in this expression. Two interesting limits with respect to the magnitude of the viscosity prove useful to characterize marginal stability. As before, we maximize instability by assuming $\gamma = 1$ and $k_z = 2\pi/H$.

3.2.1   Low viscosity limit:

First consider the limit where $\nu k_z^2 \ll \kappa$. In this case, Eq. (13) reduces to $\eta k^2 = (2\Omega S/\kappa^2)V_A k_z$ (where $\eta k_z^2 \ll \kappa$ has been self-consistently used), which, using the Lundquist number defined as $Lu = Rm\beta^{-1/2}$, can be recast as

$$Lu = \left(\frac{2\pi}{3^{1/2}} \right) \simeq 3.6. \qquad (14)$$

Note that our definition of the Lundquist number is not

strictly identical to Turner et al. (2006) but is widely used in the MHD community[2] In this regime, the $\omega_\eta^2 \kappa^2$ term balances the $2\Omega S V_A^2 k_z^2$ term in the dispersion relation Eq. (11). Eq. (14) corresponds to the limit found by Fleming et al. (2000). It is also related to the origin of the "dead zone" in accretion disks (see e.g Gammie 1996). This marginal stability limit is relevant to disks with low Prandtl numbers ($Pm \ll 1$) and high Reynolds numbers ($Re \gg 1$), such as YSO disks.

Also, for negligible resistivity, growth rates in this regime are given by

$$\tau^{-1} \simeq \frac{1}{2\pi} \left(\frac{2\Omega S}{\kappa^2} \right) V_A k_z. \qquad (15)$$

This result is valid for $V_A k_z \lesssim \kappa$ due to our expansion scheme; it also gives the correct order of magnitude of maximum growth rates when $V_A k_z \sim \kappa$, as shown by the standard dissipationless MRI analysis.

3.2.2   High viscosity limit:

Conversely, consider the large viscosity limit, where $\nu k^2 \gg \kappa$. The corresponding relations in this limit are

$$ReRm = \frac{3^{1/2}}{2}(2\pi)^3 \beta^{1/2} \simeq 215\beta^{1/2}. \qquad (16)$$

and

$$\tau^{-1} \simeq \frac{1}{2\pi} \left(\frac{2\Omega S}{\nu k_z^2} \right) V_A k_z. \qquad (17)$$

In this regime, the $\omega_\nu^2 \omega_\eta^2$ term balances the $2\Omega S V_A^2 k_z^2$ term in the dispersion relation Eq. (11). The growth rates relevant here are much smaller than in the small viscosity limit, Eq. (15). In fact, Eq. (13) indicates that this is the case as soon as $\nu k_z^2 \lesssim \kappa$, or equivalently, for the largest mode, when

$$Re \gtrsim 3(2\pi)^2/2 \simeq 60. \qquad (18)$$

This limit divides the low and high viscosity regime.

The marginal stability limit Eq.(16) obtains for large Prandtl and small Reynolds numbers. In the large Prandtl ($Pm \gg 1$) and large Reynolds number limit ($Re \gg 1$) expected in AGN disks, the growth rates of Eq. (15), or more generally of dissipationless MRI, are recovered. As before, these growth rates are expected to be valid (in order of magnitude) for $V_A k_z \lesssim \kappa$ due to our expansion scheme.

Note finally that a similar analysis can be performed for the inertial modes, but is not very informative; the damping of these modes is dominated by viscous dissipation, as these are mostly driven by the epicyclic motion.

---

[2] The difference lies in the fact that our calculation is made in the limit of high β, leading to a linear growth rate controled by V_A instead of Ω

Impact of dimensionless numbers on the efficiency MRI-induced turbulent transport. 5

3.2.3 High β limit:

Although we did not investigate this case in much detail, it is apparent from Eq. (11) that when $2\Omega S = V_A^2 k_z^2$ [cancellation of the last term in Eq. (11)], $\omega_\eta = 0$ is one of the solutions to the dispersion relation. At the light of our preceding analyzes, and because this equality embodies the MRI stability limit in the ideal case, as recalled above, it is apparent that this relation is the relevant limit in a small dissipation context as well, generalizing the result found for $Pm = 1$.

3.2.4 Heuristic explanation:

To explain the behavior brought to light in Eqs. (14) and (16), it is useful to recall the physical origin of the instability, as discussed, e.g., in Balbus & Hawley (2003), in the dissipation-free limit; the process is sketched on see Fig. 2, for convenience. Assume for definiteness that one starts by distorting the equilibrium velocity field in the radial direction with a sinusoidal perturbation in the vertical direction: $v_y = v_{y_0} \exp(-ikz)$. The magnetic field being frozen in the fluid will also develop a radial component [first term in the right-hand side member of the linearized induction equation, Eq. (8)]; the shear will then transform this radial field in an azimuthal one [second term in the right-hand side member of the linearized induction equation, Eq. (8)]. The resulting tension force produces a momentum transfer between fluid particles that have been moved according to the imposed velocity perturbation [second term in the right-hand side member of the linearized motion equation, Eq. (8)]. This force is destabilizing if the angular velocity decreases with radius: indeed in this case, the inner particle, moving faster than the outer one, will transfer orbital momentum to the outer one, thereby reinforcing its inward motion, an effect mediated by the Coriolis force when seen in the rotating frame. In this description, marginal stability follows when the driving mechanism is balanced by the usual tension restoring force (the piece not connected to the generation of magnetic field from the mean shear).

What does dissipation change to this picture ? For definiteness, let us focus on marginal stability and let us consider only resistive dissipation for the time being ("large" viscosity limit). In this limit, the magnitude of the velocity and magnetic fields in the various steps of the instability mechanism described above are controlled by dissipation processes so that one may again go through the preceding process step by step, assuming equilibrium at each step. The magnitude of the radial magnetic field in this context results from the balance between the motion driving and field dissipation:

$$-ikB_0 v_y = \eta k^2 b_y, \qquad (19)$$

while the shearing generation of the azimuthal field from the radial one is also balanced by resistive dissipation:

$$Sb_y = \eta k^2 b_x. \qquad (20)$$

Both relations follow from the induction equation in the marginal stability limit, except for the term dropped in Eq. (20), which leads to the usual magnetic tension sta-
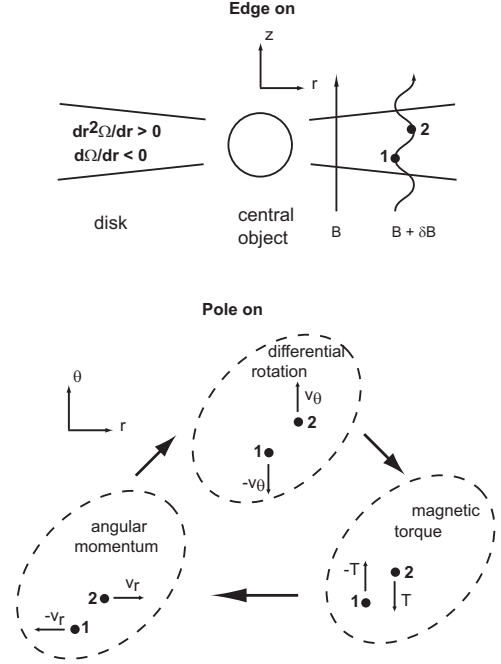

Figure 2. Sketch of the MRI mechanism (see text).

bilization and is of no interest in the limit considered here. The azimuthal force balance then requires that

$$(2\Omega - S)v_y = -i\frac{kB_0}{\mu_0 \rho_0} b_y, \qquad (21)$$

i.e., $\omega_\eta^2 \kappa^2 = 2\Omega S V_A^2 k^2$, once the two preceding constraints are taken into account (inclusion of ω in this line of argument does not change the result). As noted earlier, this relation directly leads to Eq. (14).
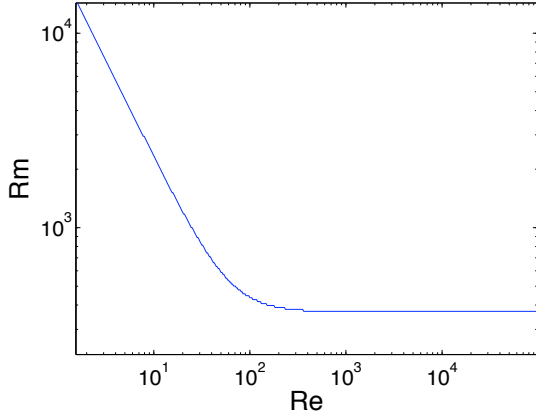
If one assumes instead that viscous dissipation exceeds the Coriolis force in magnitude, then the magnetic tension due to the generation of azimuthal field from the radial one by the shear should be balanced by viscous dissipation instead of the Coriolis force in the two horizontal components of the momentum equation, leading alternatively to $\omega \eta^2 \omega_\nu^2 = 2\Omega S V_A^2 k^2$, i.e. to Eq. (16).

This also relates to the structure of MRI modes. In the limit of a very small magnetic tension restoring force, the Alfvénic branch is made of b_y dominated modes. The other components of the magnetic field and the velocity field are of the order of $V_A k$ compared to b_y. Therefore, the growth rate is at first controlled by the dissipation rate of b_y, which is related to the resistivity [first term of the right hand side of Eq. 13]. The interaction of the other fields, which leads to the MRI, is controlled by a term symmetric in ν and η [second term of Eq. 13)].

3.2.5 Generic behavior:

A more complete view of the stability limits and growth rates implied by Eq. (11) may be obtained from exact numerical solutions for $Pm \neq 1$. Expressing this dispersion

6   *Lesur, G. and P-Y. Longaretti*

Figure 3. MRI linear stability limit in the $Pm \neq 1$ case for $\beta = 10^4$.

Figure 4. MRI growth rate (arbitrary unit) as a function of viscous and resistive dissipation for $\beta = 10^4$

relation in terms of ω leads to the condition:

$$
\begin{aligned}
\omega^4 \quad &-2ik^2\omega^3(\eta + \nu) - \omega^2\Big(a + k^4(\eta^2 + \nu^2 + 4\eta\nu) + b\Big) \\
&+\omega\Big(2ik^6(\eta\nu^2 + \nu\eta^2) + aik^2(\nu + \eta) + 2ib\eta k^2\Big) \\
&+\nu^2\eta^2k^8 + a\nu\eta k^4 + b\eta^2 k^4 - c = 0,
\end{aligned}
\tag{22}
$$

with

$$
\begin{aligned}
a &= 2k_z^2 V_A^2 &\tag{23}\\
b &= \kappa^2\gamma^2 &\tag{24}\\
c &= k_z^2 V_A^2(2\Omega\gamma^2 S - k_z^2 V_A^2) &\tag{25}
\end{aligned}
$$

To characterize the stability limits as a function of the Reynolds and the Magnetic Reynolds number ($Rm = SH^2/\eta$), one needs to choose β, γ and k_z. As in the $Pm = 1$ case, we take $k_z = 2\pi/H$ and $\gamma = 1$ (which are again expected to maximize the dissipation limits), and solve the relation (22) for $\beta = 10^4$. The resulting stability limits are shown on Fig. 3 and the corresponding growth rates on Fig. 4 (arbitrary units). These results match closely the analytical limits just discussed : a high Re threshold found for $Rm \sim 371$, and a low Re threshold found for $RmRe \sim 2.3 \times 10^4$, both in agreement with Eqs. (14) and (16), respectively. Moreover, significantly lowered growth rates are observed when $Re \ll 60$ to 80, as predicted by Eqs. (17) and (18). A similar behavior follows at much smaller β. For example, the observed scalings are identical, and the preceding asymptotic expressions valid within a factor of 2, down to β values of the order of twice the critical β limit.

These results indicate that most of the stability limit behavior is captured by the approximate relations Eqs. (14) and (16) (as well as by the large field β limit, where relevant), whose physical origin has been discussed above.

3.3   Numerics

3.3.1   Equations

Our objective is to simulate the system of Eqs. (1) and (2), with the incompressiblity condition Eq. (3), to characterize

the dependence of turbulent transport on the main dimensionless numbers introduced above (β, Re and Pm). We focus on incompressible motions; indeed, the values of α found in previous investigations makes us *a priori* expect that compressibility effects will be small. In any case, this allows us to more effectively distinguish the effects of the various physical mechanisms at work in this problem.

First, we simplify the problem from a numerical point of view by distinguishing the mean laminar shear $\boldsymbol{u} = Sy\boldsymbol{e_x}$ from the deviation from this mean $\boldsymbol{w}$. The resulting equations read:

$$
\begin{aligned}
\partial_t\boldsymbol{w} + \boldsymbol{w}\cdot\boldsymbol{\nabla}\boldsymbol{w} &= -Sy\partial_x\boldsymbol{w} - \boldsymbol{\nabla}\psi + \frac{\boldsymbol{B}\times(\boldsymbol{\nabla}\times\boldsymbol{B})}{\mu_0\rho_0} \\
&\quad +(2\Omega - S)w_y\boldsymbol{e_x} - 2\Omega w_x\boldsymbol{e_y} + \nu\Delta\boldsymbol{w} \\
\partial_t\boldsymbol{B} + \boldsymbol{w}\cdot\boldsymbol{\nabla}\boldsymbol{B} &= -Sy\partial_x\boldsymbol{B} + \boldsymbol{B}\cdot\boldsymbol{\nabla}\boldsymbol{w} + B_y S\boldsymbol{e_x} + \eta\Delta\boldsymbol{B} \\
\boldsymbol{\nabla}\cdot\boldsymbol{w} &= 0 \\
\boldsymbol{\nabla}\cdot\boldsymbol{B} &= 0
\end{aligned}
$$

This system is numerically solved using a full 3D spectral code, using the classical shearing sheet boundary conditions (Hawley et al. 1995). This code is now briefly described.

3.3.2   Numerical code

The code used for these simulations is an MHD extension of the HD code used in Lesur & Longaretti (2005), and extensively described there. This code is a full 3D spectral (Fourier) code, based on FFTW libraries, parallelized using the MPI protocol. This kind of code has many advantages for the simulation of incompressible turbulence, such as:

• The incompressibility and solenoid conditions are easily implemented at machine precision, using a projector function in the Fourier space.
• The energy budget is much easier to control, leading to a precise quantification of the energy losses by numerical dissipation.
• Spatial derivatives are very accurate down to the grid scale (equivalent to an infinite order finite difference scheme down to the grid scale).

Impact of dimensionless numbers on the efficiency MRI-induced turbulent transport.   7
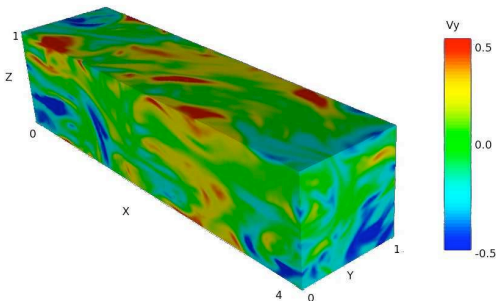
Figure 5. w_y plot (radial velocity) for $\beta = 100$, Re=3200,

The algorithm used is a classical pseudo spectral method which may be described as follows. All the derivatives are computed in Fourier space. However the nonlinear term require special treatment : in Fourier space, a real space product is a convolution, for which the computational time evolves as n^2, where n is the number of grid cells. The computation time is minimized if one goes back to real space, compute the needed product and then transforms the result to Fourier space. This procedure (pseudo spectral procedure) is more efficient than a direct convolution product since the FFT computation time scales as $n \log n$. However, the finite resolution used in this procedure generates a numerical artifact commonly known as the "aliasing" effect (apparition of non physical waves near the Nyquist Frequency). This effect may be handled through a dealiazing procedure, in which the nonlinear terms are computed with a resolution 3/2 higher than the effective resolution used in the source terms (e.g., Peyret 2002).

Comparing our spectral code with a ZEUS-type finite difference code (Stone & Norman 1992), similar results are obtained with a finite difference resolution two to three times higher than the spectral resolution. However, FFTs calculations are more computationally expensive than finite differences, leading to a final computational time equivalent for both kind of code with the same "effective" resolution.

All the simulations presented in this paper were performed with an xyz resolution of $128 \times 64 \times 64$ with an aspect ratio of $4 \times 1 \times 1$, x being the azimuthal direction, y the radial direction and z vertical direction. One may change the physical viscosity and resistivity as well as the magnetic field intensity (β). The mean magnetic field (conserved in the simulations due to the adopted boundary conditions) is aligned in the z direction. White noise initial perturbations with respect to the laminar flow are introduced as initial conditions on all variables. With $\beta = 100$, $Pm = 1$ and $Re = 3200$ one typically generates flow snapshots as shown on Fig. 5 after relaxation of transients; this flow is quite characteristic of a fully developed 3D turbulent field [3].

---

[3] Movies of some of the simulations presented in this paper may be found on the web at
http://www-laog.obs.ujf-grenoble.fr/public/glesur/index.htm

3.4   MRI behavior near the instability threshold

The MRI is a weak magnetic field instability, which should be quenched for $\beta \simeq 1$ in astrophysical disks. Since the MRI is assumed to be the source of momentum transport in disks, and as at least some such disks are expected to be close to equipartition if they are to support magnetically driven ejection (Ferreira 1997), on may wonder if this instability is efficient enough in the vicinity of near the strong magnetic field stability threshold. We investigate this question in an unstratified context here (the absence of stratification significantly raises the β stability threshold).

We present two simulations, one made at $\beta = 100$ and $Re = 3200$ (run 1) which compares to typical results one can find in the literature, and a simulation made close the β threshold, i.e. for $\beta = 30$ and $Re = 3200$ on figs (6) and (7). One immediately notes a strong difference between these two simulation. On run 1, we find a classical MRI behavior, as studied by Hawley et al. (1995), characterised by $\alpha \sim 10^{-1}$ and random variations in all the statistical quantities. However, run 2 exhibits strong exponential growth ("bursts") for about 100 shear times ($\sim$10 orbits), and a sudden drop of fluctuation amplitudes. This behavior is explained as follows : for such low β only the largest wavelength mode is unstable (and not smaller scales), which is then allowed to grow for many shear times, as this mode is an exact nonlinear solution to the incompressible equations of motions (Goodman & Xu 1994). We therefore observe the growth of the channel flow as seen by Hawley & Balbus (1992). However, as this channel solution reaches large amplitude, secondary instabilities such as the Kelvin-Helmoltz instability quickly destroys this channel flow solution once they are triggered, and a new cycle starts (see Goodman & Xu (1994) for a detailed description of these secondary instabilities).

Note that this kind of explanation may also apply to the low Reynolds threshold, since there the smallest scales are viscously damped and only the largest ones remain unstable. Indeed, we did observe this behavior close the low Reynolds threshold, as did Fleming et al. (2000) but in an indirect way (see Figs. 2 and 4 of their paper), and one can conclude that these bursts are characteristic of a marginally unstable MRI. Such bursts may be astrophysically relevant. Indeed, one may question the MRI behavior close to the dead zone (Gammie 1996), in which the magnetic Reynolds number is assumed to be low enough to damp the instability. If these bursts exist in real disks, they may quickly destroy this dead zone under the effects of the strong turbulent motions observed in our simulations.

Let us have a closer look on these bursts with the help of correlation lengths defined as

$$L_i = \frac{\int dy_i \int f(x_i) f(x_i - y_i) dx_i}{\int f^2(x_i)\, dx_i} \qquad (26)$$

where $i = 1, 2, 3$ is the direction of the correlation and f refers either to the velocity or magnetic field. Note that with this definition, the correlation length vanishes for a pure sinusoidal signal; therefore, these correlation lengths provide us with a convenient tool to follow the presence of the channel flow solution in our simulations. We show on fig. 8 and fig. 9 the evolution of the correlation length in the y and z direction for the w_x field (a similar behavior is obtained

8   *Lesur, G. and P-Y. Longaretti*
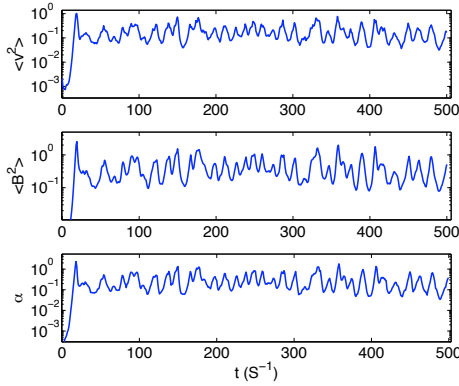

Figure 6. $\beta = 100$, Re=3200 run
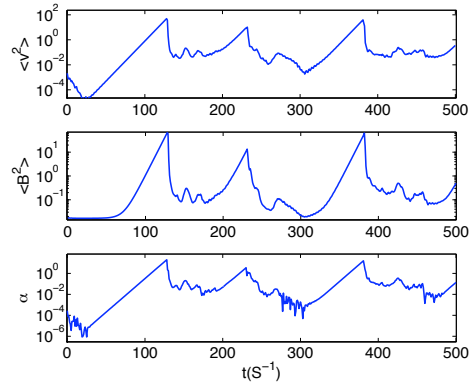
Figure 7. $\beta = 30$, Re=3200 run

with the other field components). The behavior of correlation lengths closely follows what can be seen by monitoring the energy in the deviations from the laminar flow (fig. 7), and indicate the presence of two main regimes in this simulation. The first regime corresponds to an exponential growth ("burst") of the channel flow, for which L_y is found to be equal to the box size and $L_z = 0$ (a careful examination shows that L_z is exponentially decaying down to 10^{-10}), indicating the presence of a purely sinusoidal mode in the z direction in the burst stage. The second regime is a more classical state for 3D turbulent motion, with $L_y \simeq 0.5$ and $L_z \simeq 0.4$. Note that L_y grows on very short time-scales, leading eventually to a new burst stage.

These correlation lengths also disclose some numerical artifacts present in the first regime. First, the correlation length in the y direction is artificially limited to $L_y = 1$ as a consequence of the shearing sheet boundary conditions in a finite box size. In a real disk, one would expect a loss of correlation in the radial direction on a scale of the order of a few scale heights: indeed, the typical frequency involved in these phenomena is of the order of the Keplerian frequency and a signal can't propagate faster than the sound speed, leading to a maximum correlation length of a few scale heights.

Similarly, the vanishingly small vertical correlation length for the channel flow solution is also an artifact of the adopted boundary conditions. A more realistic result would follow if one were to take into account the vertical stratification and set the boundary conditions far from the disk midplane. More generally, our results are probably not directly applicable to a real disk, but they shed some light on what the generic behavior of the MRI would look like near various stability thresholds, even though different aspect ratio and boundary conditions should be investigating before firm conclusions can be drawn.

Finally, the behavior exemplified in our simulations suggests that assuming α constant would poorly represent the transport behavior close enough to the marginal stability limit. Time-dependent transport models are needed in such a context. Real disks may not operate close to the strong field limit unless some (unknown) back-reaction loop is at work, or unless (more realistically) the magnetic field varies in a systematic way with radius throughout the disk; con-
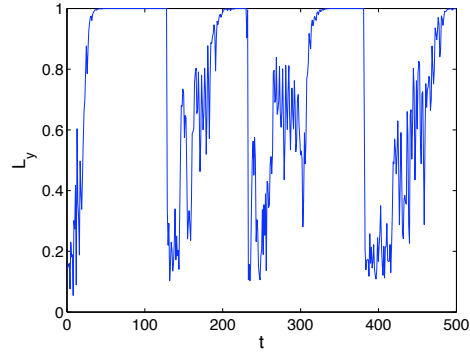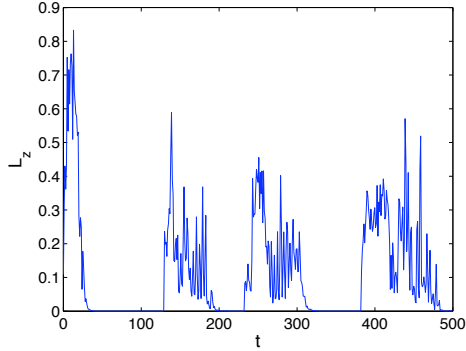

Figure 8. Correlation length of w_x in the y direction as a function of time, $\beta = 30$.

sequently, the bursting behavior observed here may imply a similar ejection variability in the relevant regions of jet-driving disks. Note however, that our "mean" equivalent α is rather large ($\alpha \simeq 5$), leading to question of the role of the ignored fluid compressibility in these cases; it is quite possible that coupling to compressible modes may effectively limit the magnitude of the bursts.
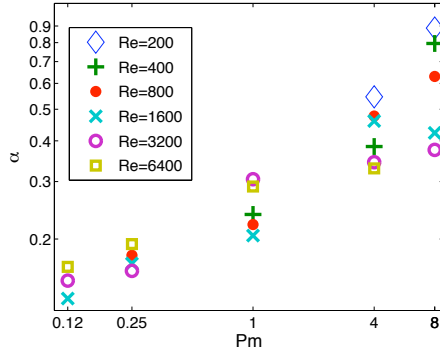
3.5   Magnetic Prandtl effect on transport coefficients

All previously published simulations were performed without exerting numerical control on the dissipation scales and dissipation processes. However, small scales have an impact on large scales processes, and therefore on transport efficiency. In this section, the role of the Reynolds and Prandtl numbers defined in section 3 is examined. In particular, the Prandtl number allows us to change the ratio of the viscous and resistive dissipation scales. Unfortunately, deviations from $Pm = 1$ are quite demanding numerically, since one wants to resolve both the velocity and magnetic dissipations scales. We present on Fig. 10 the result of such simulations: we plot the mean transport coefficient (α) as a function of the Prandtl number, for various Reynolds num-

Impact of dimensionless numbers on the efficiency MRI-induced turbulent transport. 9

Figure 9. Correlation length of w_x in the z direction as a function of time, $\beta = 30$.

Figure 11. Linear growth rate of the largest mode for various (Re, Pm) at $\beta = 100$
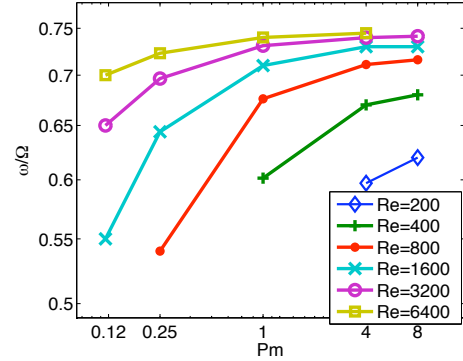

Figure 10. Prandtl effect for $\beta = 100$

bers (the Reynolds number quantifies the viscous dissipation scale). Statistical averages are computed over 500 shear times, and start after the first 100 shear times to avoid pollution by relaxation of the initial transient dynamics. From these plots, one finds a significant correlation between the Prandtl number and the transport coefficient, leading to

$$\alpha \propto Pm^\delta \qquad \text{for} \begin{cases} 0.12 < Pm < 8 \\ 200 < Re < 6400 \end{cases}, \qquad (27)$$

with δ in the range 0.25 — 0.5. Note that this result shows that the transport coefficient depends on Re and Rm via Pm, at least in the Pm range concidered in this paper. This may be seen on Fig. 10 as a small vertical dispersion (variation of both Re and Rm at constant Pm) compared to the effect of a single Pm change. Although this section is the briefest of the paper, this result constitutes the most important finding of this investigation (and the most computationally intensive one!).

Note that the numerical results obtained at very high Reynolds number and high Prandtl number are poorly resolved, mainly because of a very short magnetic dissipation scale. This remark may explain that the two points at $Pm = 8$ lie somewhat below the mean of the other results. Our preliminary tests at higher resolution seem to show that

a higher transport obtains at higher resolution at $Pm = 8$ and $Re = 6400$, which confirms a limit due to resolution in these high Pm runs. This behavior is easily understood, since the finite numerical resolution enforces a numerical dissipation scale (roughly equal to the grid scale), which is obviously the same for the magnetic and velocity fields. Therefore, at high Pm, the effective magnetic dissipation scale is forced to be larger than the expected one, leading to an altered spectral distribution and a smaller "numerical Prandtl".

One may wonder if this effect may be correlated to the linear growth rate studied before. Indeed, we plot the linear growth rate of the largest mode for the different simulations used for this study on Fig. 11. Note that one gets similar plots replacing the largest mode growth rate by the maximum growth rate. Although the idea of a transport efficiency controlled by the linear growth rate is widely spread in the Astrophysical community, this plot shows us that, at least for this example, the linear growth rate doesn't explain the transport behaviour observed on Fig. 10. Moreover, it appears that, as one may suspect from equation (13), the growth rate is not controlled only by Pm, but also by some complicated combination of Re and Rm. Umurhan et al. (2007) tries to get this kind of $alpha - Pm$ correlation analytically, using a weakly non linear analysis of the channel flow. This study leads to a stronger $\alpha - Pm$ correlation with $\delta = 1$ in the limit $Pm \ll 1$, which appears to be quite different from our full 3D numerical results. Therefore, one needs to find some full nonlinear theory to explain the transport dependance on Pm.

The correlation observed indicates the existence of a back-reaction of the small magnetic field scales on the large ones (at least for the range of Reynolds and Prandtl numbers explored here), which enhances the transport on large scales. Note that this effect is expected to saturate at some Pm, since in the limit $Pm \rightarrow 0$ with $Re \rightarrow \infty$ and Rm kept constant, equation (27) predict a null transport despite of the existence of the linear instability. Therefore, the exact implications of these findings remain to be understood, but may potentially be quite important since the Prandtl number varies by many orders of magnitude in astrophysical objects. For example, Brandenburg & Subramanian (2005)

10 *Lesur, G. and P-Y. Longaretti*

suggest that values as small as $Pm \sim 10^{-8}$ might be found in young stellar objects, while $Pm \sim 10^4$ would be more typical of AGN disks. Such a wide span is of course out of reach of present day computers.

Finally, this kind of back-reaction points out the potential role of small scale physics (dissipation scales) on the properties of turbulence at the largest available scales (disk height scale). This argues for a careful treatment of the role of dissipation and reconnection processes on the turbulence transport characterization.

4 DISCUSSION

In this paper, we have investigated the role of local dimensionless numbers on the efficiency of the dimensionless turbulent transport. To this effect, we have first generalized the previously published linear stability limits, to account for the presence of both viscous and resistive dissipation. Namely, we have confirmed in all cases that the large field marginal stability limit is characterized by a constant plasma β parameter, of order 30 in the shearing sheet unstratified context (but more likely of order unity in real, stratified disks). When marginal stability follows from dissipation and not magnetic tension stabilization, we have found that the marginal stability limit is captured by two asymptotic regime: a large Reynolds (Re), small magnetic Reynolds one (Rm), with a marginal stability limit $Rm \sim \beta^{1/2}$, and a small Reynolds, large magnetic Reynolds number one, where $ReRm \sim 10^2 \beta^{1/2}$. A phenomenological explanation has been provided for this behavior.

In the previous section, we investigated the behavior of the MRI near the low β instability threshold; in our simulations, $\beta = 30$, a value representative of the large field threshold in our simulation box. In vertically stratified disks, this threshold obtains for much smaller values, typically $\beta \sim 1$ (Gammie & Balbus 1994). We found, somewhat surprisingly, that turbulent transport is significantly enhanced through burst events, even surprisingly close to the marginal stability threshold. As pointed out earlier, this behavior is physical and not numerical. The use of periodic boundary conditions (vertical) or semi periodic (radial) boundary conditions may enhance the role of the channel flow solution which is responsibly for this behavior, and a real disk channel flow may break up sooner than observed in our local simulations, leading to smaller burst magnitudes. Moreover, $\alpha > 1$ leads to supersonic motions and compressible numerical simulations are needed to properly quantify the phenomenon, which may exhibit new secondary compressible instabilities in such a context. All these issues lead to the conclusion that low β MRI would produce weaker bursts and therefore smaller transport coefficient than observed in our simulation. However, there is no physical reason why the turbulence bursts would be suppressed, and we believe that these bursts may be a strong signature of regions of stratified disks where MRI-driven turbulence is driven close to the marginal stability threshold.

The most important new result reported in this paper is a correlation between the transport efficiency, and the magnetic Prandtl number, leading to a higher transport coefficient for larger Prandtl numbers. As in the case of the bursting behavior discussed above, the boundary conditions used in these simulations play some role in the result. However, the possible biases are less obvious and tests with plane radial walls need to be performed to get a grasp on boundary condition effects. Moreover, one needs to check the correlation at higher resolutions, and if possible higher Prandtl numbers, using different kind of codes to get a better characterization and a physical description of the phenomena involved in this observation.

More specifically, a puzzling fact points towards a potential bias due to the shearing sheet boundary conditions. In non-magnetized shear flows, transport in the subcritical regime, far enough from the marginal stability limit scales like $1/Rg$ where Rg is the subcritical transition Reynolds number (Lesur & Longaretti 2005). Closer to the marginal stability limit, and in the supercritical regime (e.g., when the Rayleigh stability criterion is not satisfied), transport is enhanced with respect to this scaling, but one always has $\alpha < 1/Rc$ where Rc is the critical Reynolds number of linear instability. However, for MRI-driven turbulence, one has $\alpha > 1/Rc$, as can be checked from our results. Close to the marginal stability limit, this enhanced efficiency is related to the existence of the channel flow solution, as discussed above. As each linear mode is a nonlinear solution to the incompressible problem, one may ask whether this enhanced transport, which is observed also far from the marginal stability limit, is not an artifact of the shearing sheet boundary condition, which allows such nonlinear coherent modes to develop. This behavior is not necessarily unphysical or irrelevant to actual disk systems, but this point needs to be checked in the future.

Finally, let us come back to the magnetic Prandtl number behavior. As pointed out earlier, the dependence of the transport efficiency on the magnetic Prandtl number indicates a back-reaction of small scales on large ones. We make here a few comments on this feature. The magnetic Prandtl number is related to the ratio of the viscous l_ν and resistive l_η dissipation scales, the exact relation depending on the shape of the turbulent energy spectrum. Generally speaking, the Prandtl number varies monotonically with the ratio l_ν/l_η, and one expects $Pm \ll 1$ (resp. $Pm \gg 1$) when $l_\nu/l_\eta \ll 1$ (resp. $l_\nu/l_\eta \ll 1$). The spectrum of the largest scales tends to be flatter than usual turbulent spectra due to the role of the linear instability, down to the scale where the magnetic tension prevents the instability to occur (most probably, this "instability section" of the spectrum only represents a small part of the overall turbulent spectra of actual disks, because of their enormous Reynolds numbers). Leaving aside these largest scales, for $Pm \ll 1$, the spectrum is expected to be Kolmogorovian and anisotropic down to the resistive dissipation scale (Goldreich & Sridhar 1995), while below this scale and down to the viscous scale, the velocity spectrum is the usual Kolmogorov velocity spectrum and the magnetic spectrum drops much faster. On the other hand, for $Pm \gg 1$, the spectrum should be Kolmogorovian down to the viscous dissipation scale (Goldreich & Sridhar 1995), while the magnetic spectrum should scale like k^{-1} below the viscous dissipation scale and down to resistive scale (Cho et al. 2003). It is therefore tempting to see in a difference of accumulation of magnetic energy at small scales the cause of the back-reaction of these scales to the largest ones, which would create the observed magnetic Prandtl number dependence of the turbulent transport efficiency. Neverthe-

Impact of dimensionless numbers on the efficiency MRI-induced turbulent transport. 11

less, in both small and large Prandtl number settings, turbulent motions in the inertial range are random in phase, so that one expects that to lowest order, coupling of the turbulent spectrum with the largest MRI unstable scales vanishes. To next order, the steepness of the Kolmogorov spectrum indicates that the strength of the coupling decreases with increasing Reynolds number in the vicinity of the viscous dissipation scale, suggesting that at large enough Reynolds number, the Prandtl dependence should saturate, especially on the large Prandtl number side. Such a saturation was not observed in our simulations, although a weak dependence of our results on the magnitude of the Reynolds number may be detected on Fig. 10; however, such an effect might also arise from resolution requirements, which makes our lower Reynolds number results confined to the larger Prandtl number range. Unfortunately, our results can hardly be improved upon with the present generation of computers, leaving the question of the Reynolds number saturation of the Prandtl number dependence open, as well as the overall difference in transport efficiency between the small and large Prandtl number cases. Resolving this issue is crucial to ascertain the role of the magneto-rotational instability in disk transport.

REFERENCES

Arlt R., Urpin V., 2004, A&A, 426, 755
Balbus S. A., 2003, ARA&A, 41, 555
Balbus S. A., Hawley J. F., 1991, ApJ, 376, 214
Balbus S. A., Hawley J. F., 2003, in Falgarone E., Passot T., eds, LNP Vol. 614: Turbulence and Magnetic Fields in Astrophysics Numerical Simulations of MHD Turbulence in Accretion Disks. pp 329–348
Balbus S. A., Hawley J. F., Stone J. M., 1996, ApJ, 467, 76
Balbus S. A., Terquem C., 2001, Astrophys. J., 552, 235
Blaes O. M., Balbus S. A., 1994, Astrophys. J., 421, 163
Brandenburg A., Nordlund A., Stein R. F., Torkelsson U., 1995, ApJ, 446, 741
Brandenburg A., Subramanian K., 2005, Phys. Rep., 417, 1
Cho J., Lazarian A., Vishniac E. T., 2003, ApJ, 595, 812
Dubrulle B., Marié L., Normand C., Richard D., Hersant F., Zahn J.-P., 2005, A&A, 429, 1
Ferreira J., 1997, A&A, 319, 340
Fleming T. P., Stone J. M., Hawley J. F., 2000, ApJ, 530, 464
Gammie C. F., 1996, ApJ, 457, 355
Gammie C. F., Balbus S. A., 1994, MNRAS, 270, 138
Gardiner T. A., Stone J. M., 2005, in de Gouveia dal Pino E. M., Lugones G., Lazarian A., eds, AIP Conf. Proc. 784: Magnetic Fields in the Universe: From Laboratory and Stars to Primordial Structures. Energetics in MRI driven Turbulence. pp 475–488
Goldreich P., Sridhar S., 1995, ApJ, 438, 763
Goodman J., Xu G., 1994, ApJ, 432, 213
Hawley J. F., 2000, ApJ, 528, 462
Hawley J. F., Balbus S. A., 1992, ApJ, 400, 595
Hawley J. F., Balbus S. A., Winters W. F., 1999, ApJ, 518, 394
Hawley J. F., Gammie C. F., Balbus S. A., 1995, ApJ, 440, 742
Ji H., Burin M., Schartman E., Goodman J., 2006, Nature, 444, 343
Ji H., Goodman J., Kageyama A., 2001, MNRAS, 325, L1
Johnson B. M., Gammie C. F., 2006, ApJ, 636, 63
Klahr H. H., Bodenheimer P., 2003, ApJ, 582, 869
Lesur G., Longaretti P.-Y., 2005, A&A, 444, 25
Longaretti P.-Y., Lesur G., 2007, In preparation for A&A
Peyret R., 2002, Spectral Methods for Incompressible Viscous Flow. Springer
Richard D., 2001, PhD thesis, Université de Paris VII
Richard D., Dauchot O., Zahn J.-P., 2001, in Proc. of the 12th Couette-Taylor Workshop, Evanston, USA Subcritical Instabilities of Astrophysical Interest in Couette-Taylor System
Richard D., Zahn J., 1999, A&A, 347, 734
Rüdiger G., Shalybkov D., 2002, Phys. Rev. E, 66, 016307
Shakura N. I., Sunyaev R. A., 1973, A&A, 24, 337
Shalybkov D., Ruediger G., 2005, A&A, 438, 411
Stone J. M., Hawley J. F., Gammie C. F., Balbus S. A., 1996, ApJ, 463, 656
Stone J. M., Norman M. L., 1992, ApJs, 80, 753
Turner N. J., Sano T., Dziourkevitch N., 2006, astro-ph/0612552
Umurhan O. M., Menou K., Regev O., 2007, Phys. Rev. Let., 98, 034501
Urpin V., 2003, A&A, 404, 397
Wardle M., 1999, MNRAS, 307, 849